

---


Electronic Theses and Dissertations, 2004-2019

---

2013

## Investigation Of Multiscale Fluid Structure Interaction Modeling Of Flow In Arterial Systems

Sebastian Sotelo  
*University of Central Florida*

 Part of the [Mechanical Engineering Commons](#)  
Find similar works at: <https://stars.library.ucf.edu/etd>  
University of Central Florida Libraries <http://library.ucf.edu>

This Masters Thesis (Open Access) is brought to you for free and open access by STARS. It has been accepted for inclusion in Electronic Theses and Dissertations, 2004-2019 by an authorized administrator of STARS. For more information, please contact [STARS@ucf.edu](mailto:STARS@ucf.edu).

---

### STARS Citation

Sotelo, Sebastian, "Investigation Of Multiscale Fluid Structure Interaction Modeling Of Flow In Arterial Systems" (2013). *Electronic Theses and Dissertations, 2004-2019*. 2580.  
<https://stars.library.ucf.edu/etd/2580>

INVESTIGATION OF MULTISCALE FLUID STRUCTURE INTERACTION MODELING  
OF FLOW IN ARTERIAL SYSTEMS

by

SEBASTIAN RODRIGO SOTELO  
B.S. University of Central Florida, 2012

A thesis submitted in partial fulfillment of the requirements  
for the degree of Master of Science  
in the Department of Mechanical and Aerospace Engineering  
in the College of Engineering and Computer Science  
at the University of Central Florida  
Orlando, Florida

Spring Term  
2013

Major Professor: Alain Kassab

© 2013 Sebastian Rodrigo Sotelo

## **ABSTRACT**

The study of hemodynamic patterns in large blood vessels, such as the ascending aortic artery, brachiocephalic trunk, right carotid artery and right subclavian artery presents the challenging complexity of vessel wall compliance induced by the high levels of shear stress gradients and blood flow pulsatility. Accurate prediction of hemodynamics in such conditions requires a complete Fluid Structure Interaction (FSI) analysis that couples the fluid flow behavior throughout the cardiac cycle with the structural response of the vessel walls. This research focuses on the computational study of a Multiscale Fluid-Structure Interaction on the arterial wall by coupling Finite Volumes Method (FVM) predictions of the Fluid Dynamics within the artery with Finite Elements Method (FEM) predictions of the Elasto-Dynamics response of the arterial walls and 1-D closed loop electrical circuit system to generate the dynamic pressure pulse. To this end, a commercial FVM Computational Fluid Dynamics (CFD) code (STAR-CCM+ 7.09.012) will be coupled through an external interface with a commercial FEM Elasto-Dynamics code (ABAQUS V6.12). The coupling interface is written in such a way that the wall shear stresses and pressures predicted by the CFD analysis will be passed as boundary conditions to the FEM structural solver. The deformations predicted by the FEM structural solver will be passed to the CFD solver to update the geometry in an implicit manner before the following iteration step. The coupling between the FSI and the 1-D closed loop lump parameter circuit updated the pressure pulse and mass flow rates generated by the circuit in an explicit manner after the periodic solution in the FSI analysis had settled. The methodology resulting from this study will be incorporated in a larger collaborative research program between UCF and ORHS that entails optimization of surgical implantation of Left Ventricular Assist

Devices (LVAD) cannulae and bypass grafts with the aim to minimize thrombo-embolic events. Moreover, the work proposed will also be applied to another such collaborative project focused on the computational fluid dynamics modeling of the circulation of congenitally affected cardiovascular systems of neonates, specifically the Norwood and Hybrid Norwood circulation of children affected by the hypoplastic left heart syndrome.

I dedicate this thesis to my loving wife that supported and encouraged me throughout my education and believed in me each step of the way.

# TABLE OF CONTENTS

LIST OF FIGURES .....	vii
LIST OF TABLES .....	ix
CHAPTER 1: INTRODUCTION .....	1
CHAPTER 2: LITERATURE REVIEW .....	4
CHAPTER 3: METHODS .....	7
3.1 Computational Solid Mechanics .....	7
3.1.1 Hyperelastic model in ABAQUS .....	9
3.2 Computational Fluid Dynamics .....	15
3.3 Fluid structure interaction coupling .....	18
3.3.1 Co-simulation between ABAQUS and STAR-CCM+ .....	18
3.4 Lumped Parameter Model .....	22
CHAPTER 4: RESULTS .....	30
4.1 Comparison between Compliant vs. Compliant with Gore-Tex patch model .....	34
4.2 Comparison between Compliant vs. non-Compliant model .....	48
CHAPTER 5: CONCLUSION AND FUTURE WORK .....	56
APPENDIX: DERIVATIONS .....	57
REFERENCES .....	60

## LIST OF FIGURES

Figure 1: Contrast-enhanced MR Angiography of brachiocephalic bifurcation .....	1
Figure 2: Histomechanical idealization of a healthy elastic artery .....	7
Figure 3: Aorta 3-layer composite solid mesh.....	12
Figure 4: Bifurcation 3-layer composite solid mesh.....	13
Figure 5: Bifurcation 3-layer composite solid mesh with Gore-Tex patch .....	14
Figure 6: Aorta fluid mesh.....	17
Figure 7: Bifurcation fluid mesh.....	17
Figure 8: Coupling of FSI and Lump parameter model.....	22
Figure 9: Generic block of vascular bed compartments .....	24
Figure 10: Bifurcation 1-D cardiovascular circuit model.....	25
Figure 11: FSI couple with lump parameter model .....	25
Figure 12: Elastance Function and $-\dot{C}(t)/C(t)$ over one cardiac cycle.....	27
Figure 13: Pressure and Cardiac output .....	29
Figure 14: Innominate, Right Carotid, and Right Subclavian Artery Pressure waveform .....	31
Figure 15: Innominate, Right Carotid, and Right Subclavian Artery Flow rate waveform.....	31
Figure 16: Carotid Artery Doppler images and calculated flow rate (ml/s) waveform .....	31
Figure 17: Visualization of flow relative to Innominate artery flow rate .....	34



Figure 18: Wall Shear Stress of Compliant and Compliant-Gore-Tex.....	37
Figure 19: RSA (right subclavian artery) and RCA (right carotid artery) cross-sections .....	38
Figure 20: RCA cross-section velocity of Compliant and Compliant-Gore-Tex model .....	39
Figure 21: RSA cross-section velocity of Compliant and Compliant-Gore-Tex model.....	40
Figure 22: Velocity Field of Compliant and Compliant-Gore-Tex model .....	41
Figure 23: Streamlines velocity magnitude of Compliant and Compliant-Gore-Tex model.....	42
Figure 24: Pressure of Compliant and Compliant-Gore-Tex model.....	43
Figure 25: Strain of Compliant and Compliant-Gore-Tex model.....	44
Figure 26: Wall Shear Stress of Compliant and non-Compliant .....	50
Figure 27: RCA cross section velocity of Compliant and non-Compliant model .....	51
Figure 28: RSA cross section velocity of Compliant and non-Compliant model.....	52
Figure 29: Velocity Field of Compliant and non-Compliant model.....	53
Figure 30: Streamlines velocity magnitude of Compliant and non-Compliant model .....	54
Figure 31: Pressure of Compliant and non-Compliant model .....	55

## LIST OF TABLES

Table 1: Parameters for the Holzapfel-Gasser-Ogden model in ABAQUS .....	11
Table 2: Problem size for solid domain models.....	12
Table 3: Problem size for fluid domain models.....	16
Table 4: Left ventricle heart, aorta, and systemic model parameters .....	28
Table 5: Calculated resistance, capacitance, and inductance of arteries.....	32
Table 6: Comparison of total flow rate per cycle between models.....	32
Table 7: Calculated resistance, capacitance, and inductance of arterial and venous beds.....	33
Table 8: Von Misses Stress for Compliant model .....	45
Table 9: Von Misses Stress for Compliant with Gore-Tex model.....	45
Table 10: Displacement magnitude for Compliant model.....	46
Table 11: Displacement magnitude for Compliant with Gore-Tex model .....	46
Table 12: Wall velocity magnitude for Compliant model .....	47
Table 13: Wall velocity magnitude for Compliant with Gore-Tex model.....	47

## CHAPTER 1: INTRODUCTION

The study of a multiscale fluid structure interaction between three dimensional incompressible fluid, and anisotropic hyperelastic compliant vessels has several computational challenges. The numerical complexities that this study faces involves non-linear-anisotropic behavior of the arterial wall, non-Newtonian fluid such as blood and strong multi-physics coupling between the solid and fluid domain interfaces. The coupling will also need to handle a ratio near unity of the fluid and solid density. For this particular case the subject of study is the brachiocephalic (innominate) artery bifurcation. This thoracic artery arises from the arch of the aorta and splits into the right subclavian (RSA) and right carotid (RCA) arteries. The right subclavian artery supplies oxygenated blood to the right arm. The right carotid artery supplies oxygenated blood to the head and neck areas.



(Nael, Villablanca, Pope, Laub, & Finn, 2007)

Figure 1: Contrast-enhanced MR Angiography of brachiocephalic bifurcation

In this particular case study the behavior of the flow field of the blood and shear stress, and compliance of the arterial wall will be studied using a multiscale-fluid-structure-interaction model. The findings and methodology from this work will be used as a baseline for future projects such as optimization of surgical implantation of Left Ventricular Assist Devices (LVAD) cannulae and bypass grafts. This is with the aim to minimize thrombo-embolic events by creating the computational fluid dynamics modeling of the circulation of congenitally affected cardiovascular systems of neonates, specifically the Norwood and Hybrid Norwood circulation of children affected by the hypoplastic left heart syndrome.

In order to achieve this goal first a CAD drawing of the bifurcation for the fluid and solid domain was performed. The CAD file of the bifurcation geometry of the fluid and solid domains interfaces needed to coincide in measurements. One out of the two solid domain models was modified in order to implement a Gore-Tex patch in the right carotid artery wall. Once that was completed the geometry was imported to the respective fluid and solid domains solver. In this case STAR-CCM+ 7.09.012 would solve the fluid domain calculations and ABAQUS V.12 will solve the solid domain calculations. The multi-physics co-simulation is then performed implicitly between the fluid and solid domains by the SIMULIA Co-Simulation Engine which is ran by ABAQUS in the background. A co-simulation script needed to be added to the ABAQUS input file in order to perform the co-simulation between ABAQUS and STAR-CCM+. After that was put into place the following step was used to determine the field functions that need to be exchanged and the coupled boundaries. For this particular case the STAR-CCM+ exports static pressures and wall shear stresses to the solid domain in ABAQUS and imports the nodal displacement that ABAQUS calculates. The units of exchange also had to be determined. For

this case study the exported units from STAR-CCM+ to ABAQUS are mm and MPa. At last the compliant bifurcation model was compare with the compliant with Gore-Tex model and the non-compliant model to determine the changes in the flow field, pressure, and wall shear stress.

## CHAPTER 2: LITERATURE REVIEW

The study of a multiscale fluid structure interaction of a flexible wall with large strain deformations such as the arterial wall faces a multitude of challenges. One of the tasks involved in performing this kind of study is its numerical complexities in solving the fluid and solid interfaces continuity equations for a non-linear wall behavior and a non-Newtonian fluid. The coupling algorithm must be capable of handling the multi-physics exchange of field functions between the interfaces. The FSI also has to be coupled with a lump parameter model that updates the boundary conditions at the inlets and outlets until the periodic waveforms settles

Regarding the study of a multiscale fluid structure interaction model of an arterial wall Alistair G. Brown (Brown, et al., 2012) performed a computational study of the aortic hemodynamics of the vascular system for a patient-specific aorta. In this work three different models were studied. Each of the models was coupled with a Windkessel model (0D model) in order to prescribe boundary conditions at the boundaries. All of the models calculated the 3D-flow field using the computational fluid dynamic (CFD) commercial code ANSYS-CFX. One of the models calculated the flow field by treating the fluid as an incompressible fluid. Another model treated the fluid as a compressible fluid. The third model comprised of a fully couple fluid structure interaction (FSI). The aortic wall was treated as a linear elastic incompressible model in the FSI solid domain. The Windkessel model was solved using a first order backward Euler approach. It was applied to the CFD models in an explicit manner after every time-step (5 ms) in order to prescribe the boundary conditions. The findings of this research show that the incompressible and compressible 3D CFD calculation of the flow field take much less time (7.8

hrs and 6.8 hrs) to get an adequate answer compare to the FSI model (145.5 hrs). It also shows a higher wall shear stress at the aortic walls for the incompressible and compressible 3D CFD calculation compare to the FSI model at early, peak, late systole and mid, end diastole. The maximum WSS (Pa) for the FSI model were as follows: 6.01, 18.19, 17.72, 0.94, and 0.73 for early, peak, late systole and mid, end diastole respectably.

While Brown (Brown, et al., 2012) used a liner relation for the arterial wall Xenow (Xenow, et al., 2010) used a non-linear representation of the arterial wall. Xenow performed a fluid structure interaction for a study in the abdominal aortic aneurysm (Xenow, et al., 2010). In this study the parameters used to create the model were obtained from CT scans measurements from a selected group of patients. The purpose of this work was to examine the flow field and wall shear stress in the iliac arteries bifurcation. Different geometry parameters were used for the purpose of developing an additional diagnostic tool to assist clinicians. In this work the commercial computational code ADINA was used to perform the fluid and solid domain calculations. The fluid was treated as a Newtonian fluid and the flow as laminar. The boundary conditions prescribed in the fluid domain were a fixed velocity waveform at the inlet and pressure wave at the outlet. For the solid domain the arterial wall was modeled using two models. In one of the models the arterial wall was treated as an isotropic material using the Mooney–Rivlin model. The other model used the Holzapfel orthotropic material formulation treating the wall as an anisotropic material. The Arbitrary Lagrangian–Eulerian (ALE) approach was used for the deformation of the fluid mesh at every time step. The fluid and solid interfaces was coupled directly, and large strains deformations were used in the model. The arterial wall deformations were calculated using a linear dynamics response. Both the fluid and solid domains

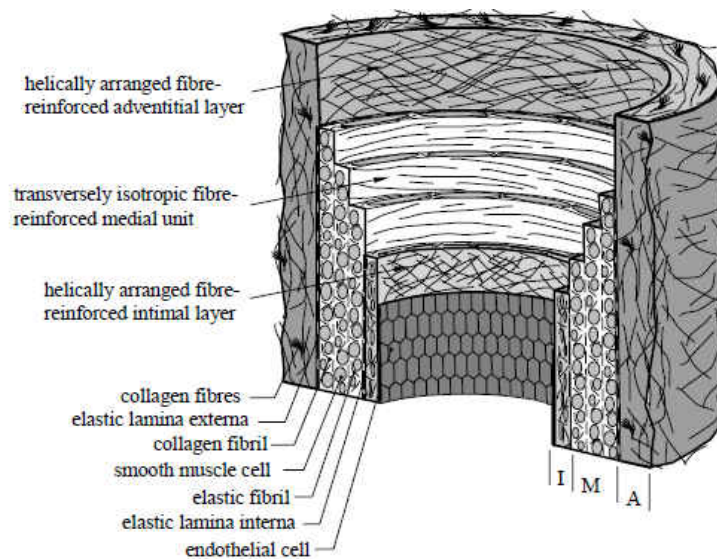
were calculated using a first order finite-element scheme. It was determined that a peak wall shear stress (WSS) of 2.66 PA was present during peak systole at a 0 degree inlet angle. It was also found that maximum velocity magnitude for the 120 degree bifurcation angle was 3% lower than the maximum velocity magnitude of the 60 degree bifurcation angle geometry.



## CHAPTER 3: METHODS

### 3.1 Computational Solid Mechanics

A multi-layer model for an arterial wall is centered on the mechanics of fiber-reinforced composites theory. It represents the symmetries of a cylindrical orthotropic material. The arterial wall is made of three major thick-walled layers (Intimia (I), media (M), and adventitia (A)).



(Holzapfel, Gasser, & Ogden, 2000)

Figure 2: Histomechanical idealization of a healthy elastic artery

Each of the layers of the arterial wall is treated as a composite reinforced by two collagen fibers. These fibers are ordered in symmetrical spirals. It is safe to assume that each layer has similar mechanical features. However they may have different set parameters that define the material. Thus the same strain-energy function can be used for each layer (Holzapfel, Gasser, & Ogden, 2000).

In order to represent the hyperelastic behavior of the arterial wall in the solid domain the Holzapfel-Gasser-Ogden built-in model in ABAQUS was used. The Holzapfel model (Holzapfel, Gasser, & Ogden, 2000) separates the strain-energy function  $\psi$  into two main parts:  $\Psi_{iso}$  and  $\Psi_{aniso}$  which associates the isotropic (non-collagenous material matrix mechanical response) and anisotropic (resistance to stretch at high pressures due to collagenous fibers). Thus the potential strain-energy function is represented as follows:

$$\psi(\bar{C}, A_1, A_2) = \Psi_{iso}(\bar{C}) + \Psi_{aniso}(\bar{C}, A_1, A_2) \quad (1)$$

Where  $\bar{C}$  represents the distortional part of the right Cauchy-Green strain (APPENDIX: DERIVATIONS), and  $A_i$  for  $i = 1, 2$  the structure tensor product of  $a_{01} \otimes a_{02}$  which are the two reference direction vectors of the collagenous fibers with  $|a_{01}| = |a_{02}| = 1$  (Holzapfel, Gasser, & Ogden, 2000). In order to represent the response of the fibers the parameters  $\bar{C}, A_1$  and  $A_2$  are describe in the following invariant-based formulation (Gasser, Ogden, & Holzapfel, 2006).

$$\bar{I}_1(\bar{C}) = \text{tr } \bar{C}, I_2(\bar{C}) = \frac{1}{2}[(\text{tr } \bar{C})^2 - \text{tr } \bar{C}^2], \text{ and } \bar{I}_3(\bar{C}) = \det \bar{C} = 1 \quad (2)$$

$$\bar{I}_4(\bar{C}, a_{01}) = \bar{C} : A_1 \quad \bar{I}_5(\bar{C}, a_{01}) = \bar{C}^2 : A_1 \quad (3)$$

$$\bar{I}_6(\bar{C}, a_{02}) = \bar{C} : A_2 \quad \bar{I}_7(\bar{C}, a_{02}) = \bar{C}^2 : A_2 \quad (4)$$

$$\bar{I}_8(\bar{C}, a_{01}, a_{02}) = (a_{01} * a_{02}) a_{01} * \bar{C} a_{02} \quad \bar{I}_9(a_{01}, a_{02}) = (a_{01} * a_{02})^2 \quad (5)$$

Since the  $\bar{I}_8$  and  $\bar{I}_9$  are constants, and  $\bar{I}_4$  and  $\bar{I}_6$  represent the stretches in the direction of  $a_{01}$  and  $a_{02}$  which is sufficient to capture the general anisotropic mechanical behavior of the arterial wall the strain-energy (1) can be reduced to

$$\psi(\bar{C}, A_1, A_2) = \Psi_{iso}(\bar{I}_1) + \Psi_{aniso}(\bar{I}_4, \bar{I}_6) \quad (6)$$

$\Psi_{iso}(\bar{I}_1)$  can be represented using the neo-Hookean model for the isotropic response in each layer as follows

$$\Psi_{iso}(\bar{I}_1) = \frac{\mu}{2}(\bar{I}_1 - 3) \quad (7)$$

Where  $\mu$  represents shear modulus of the material and  $\bar{I}_1$  is the first deviatoric strain invariant of the distortional part of the right Cauchy–Green tensor  $\bar{C}$ .

$\bar{\Psi}_{aniso}(\bar{I}_4, \bar{I}_6)$  is represented by an exponential function to describe the strain energy stored in the collage fibers

$$\bar{\Psi}_{aniso}(\bar{I}_4, \bar{I}_6) = \frac{k_1}{2k_2} \sum_{i=4,6} \{\exp[k_2(\bar{I}_i - 1)^2] - 1\} \quad (8)$$

Where  $k_1 > 0$  is a stress-like material parameter and  $k_2 > 0$  is a dimensionless parameter. These parameters do not affect the mechanical response of the arterial wall in the low pressure domain. The invariants  $\bar{I}_4$  and  $\bar{I}_6$  correspond to the square of the stretches of the fibers in the fiber directions (Holzapfel, Gasser, & Ogden, 2000).

### 3.1.1 Hyperelastic model in ABAQUS

The solid models were created using the commercial code ABAQUS v6.12 Simulia. These models were created to represent the hyperelastic properties of the arterial wall. ABAQUS

uses several models to represent the behavior of an anisotropic hyperelastic material. In this particular case the Holzapfel-Gasser-Ogden built-in model was used. This hyperelastic model combines the strain energy potential function proposed by Holzapfel, Gasser and Ogden (Holzapfel, Gasser, & Ogden, 2000) (Gasser, Ogden, & Holzapfel, 2006) to model the arterial layers with distributed collagen fiber orientations such that:

$$U = C_{10}(\bar{I}_1 - 3) + \frac{1}{D} \left( \frac{(J^{el})^2 - 1}{2} - \ln(J^{el}) \right) + \frac{k_1}{2k_2} \sum_{\alpha=1}^N \{ \exp[k_2 < \bar{E}_\alpha >^2] - 1 \} \quad (9)$$

$$\bar{E}_\alpha \stackrel{\text{def}}{=} k(\bar{I}_1 - 3) + (1 - 3k)(\bar{I}_{4(\alpha\alpha)} - 1); \bar{I}_{4(\alpha\alpha)} = A_\alpha \cdot \bar{C} \cdot A_\alpha \quad (10)$$

$$k = \frac{1}{4} \int_0^\pi \rho(\Theta) * \sin^3 \Theta d\Theta \quad (11)$$

Where  $U$  is the strain-energy potential. This functions represents the strain energy stored per unit of reference volume;  $C_{10} = \frac{\mu}{2}$ ;  $D = \frac{2}{K_0}$  ( $K_0$  initial bulk modulus);  $J^{el}$  is the elastic volume ratio;  $N$  refers to the number of families of fibers ( $N \leq 3$ ).  $\bar{I}_1$  represents the first deviatoric strain invariant as in equation (2).  $\bar{I}_{4(\alpha\alpha)}$  in (10) are the pseudo-invariants of  $\bar{C}$  and  $A_\alpha$  (modified Green strain tensor and unit vectors of the direction of the fibers).  $k_1$  and  $k_2$  are the same parameters as described in (8). The parameter  $k$  in (11) describes the level of scattering in the fiber directions (if  $k = 0$  fibers are perfectly aligned and  $k = 1/3$  fibers are randomly distributed and the material becomes isotropic). The density  $\rho(\Theta)$  is a function of the orientation of the number of fibers in the range of  $[\Theta, \Theta + d\Theta]$  (ABAQUS) (Gasser, Ogden, & Holzapfel, 2006).

The collagen fibers are only activated during tension loads since buckling could occur under compression loads. ABAQUS uses equation (9) where  $\bar{E}_\alpha > 0$  and  $< \bar{E}_\alpha > =$

$\frac{1}{2}(|\bar{E}_\alpha| + \bar{E}_\alpha)$  in order to prevent buckling in the model (ABAQUS). The D parameter in (9) is thus taken to be approximately zero (1E-6) in order to treat this model as an incompressible solid since arteries can be treated as such under physiological loads (Carew, Vaishnav, & Patel, 1968). Below table 1 shows the parameters used to model the anisotropic hyperelastic model of the thoracic aorta in ABAQUS.

Table 1: Parameters for the Holzapfel-Gasser-Ogden model in ABAQUS  
(Weisbecker, Pierce, & Holzapfel, 2012) (Lantz, Renner, & Karlsson, 2011)

Human Artery	$\mu$ (MPa)	$k_1$ (MPa)	$k_2$	$k$	$\theta$ (°)	$\rho$ ( $\frac{\text{kg}}{\text{m}^3}$ )
Thoracic Artery	Three-layer Composite					
	0.017	0.56	16.21	0.18	51.0	1080

Three different models were created, an aorta and two bifurcations (Innominate, Right Carotid Artery, and Right Subclavian Artery). The wall thickness used in the aorta model was 2.59 mm for the three-layer composite aorta (Weisbecker, Pierce, & Holzapfel, 2012). The dimensions for the aorta inner diameter and length are 18mm and 50 mm respectively. The bifurcations models dimensions were as follows: constant wall thickness of 1.3mm, inner diameters of 12.4mm for the Innominate artery, 8mm for the right subclavian artery, and 7.4mm for the right carotid artery. To one of the bifurcation models a Gore-Tex patch near the midsection of the right carotid artery was placed. The length of the Gore-Tex patch along the axis is approximately 22.8mm and 10 mm radially. The patch entails of 615 quadratic tetrahedral

elements of type C3D10 of the bifurcation model. The Gore-Tex patch was modeled with the following material properties Young's modulus of 40 MPa and density of 3.30e-09 tonne/mm<sup>3</sup> (Long, Hsu, Bazilevs, Feinstein, & Marsden, 2012). A 20-node quadratic brick was used to mesh the aorta model and a 10-node quadratic tetrahedron mesh was used to discretize the bifurcation model.

Below table 2 contains the elements, nodes and number of variable that were solved for the solid model in ABAQUS using the Holzapfel hyperelastic anisotropic built-in model and figures 2 and 3 show the mesh used for the aortas and bifurcation model.

Table 2: Problem size for solid domain models

Model	Elements	Nodes	Total Number of variables
Aorta: 3-layer-composite	2904	15718	47154
Bifurcation: 3-layer composite	11452	22567	67701

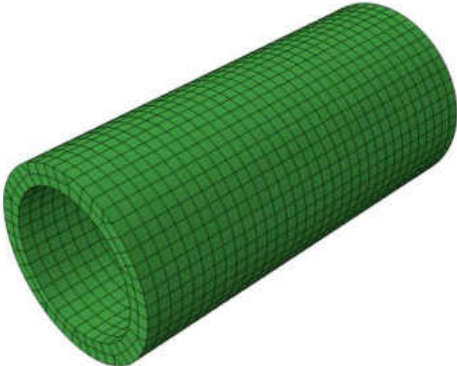


Figure 3: Aorta 3-layer composite solid mesh

The boundary conditions applied to the bifurcation solid domain (with and without Gore-Tex) were as follow: 2 mm of allowable displacement on the radial direction and fixed on the axial direction at the brachiocephalic root end face, 1.5 mm of allowable displacement on the radial direction at the right carotid artery end face, and 1.75 mm of allowable displacement on the radial direction at the right subclavian artery end face (APPENDIX: DERIVATIONS). The boundary conditions were referenced to a local coordinate system created at the center of each of the faces. The solid domain was solved using ABAQUS dynamic-quasi-static solver with a velocity parabolic extrapolation.

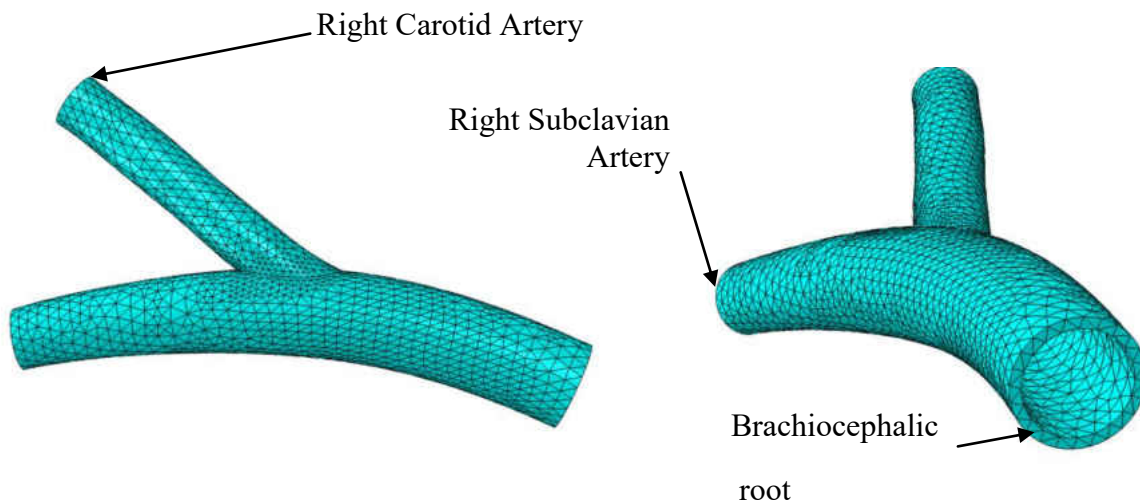


Figure 4: Bifurcation 3-layer composite solid mesh

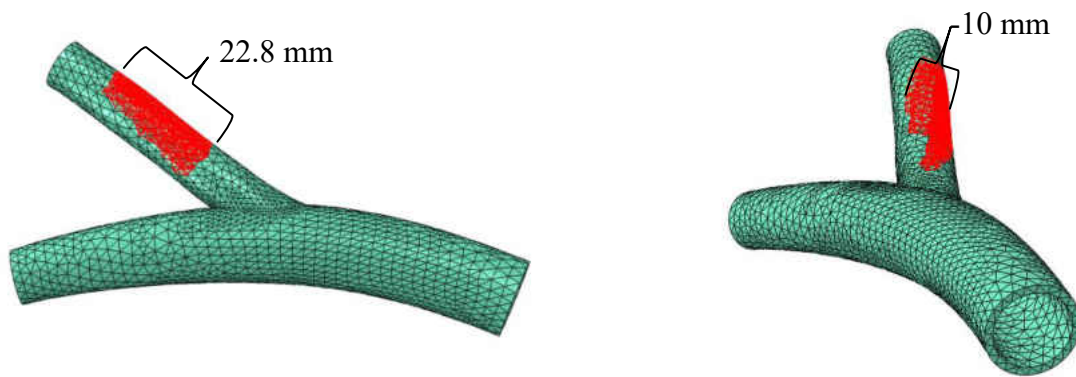


Figure 5: Bifurcation 3-layer composite solid mesh with Gore-Tex patch



### 3.2 Computational Fluid Dynamics

The segregated flow formulation was used in STAR-CCM+ to solve the continuity and momentum governing equations. For this particular model the fluid (blood) was treated as Laminar, Newtonian and incompressible fluid with a constant density of 1060 kg/m<sup>3</sup> and a dynamic viscosity of 0.004 Pa-s. Gravitational forces were neglected.

$$\nabla \cdot \vec{V} = 0 \quad (12)$$

$$\rho \frac{\partial \vec{V}}{\partial t} + \rho(\vec{V} \cdot \nabla)\vec{V} = -\nabla p + \mu \nabla^2 \vec{V} \quad (13)$$

The governing equations were discretized using a Finite Volume Discretization method. For the momentum equation applying a cell-centered control volume for cell-0:

$$\frac{\partial}{\partial t}(\rho \chi v V)_0 + \sum_f [v \rho (v - v_g) \cdot a]_f = -\sum_f (p I \cdot a)_f + \sum_f T \cdot a \quad (14)$$

Where the left hand side of (14) represents the transient terms and convective flux. The right hand side represents the pressure gradient, viscous flux and the body force terms. T in (14) is the viscous stress tensor. T is equal to the laminar stress tensor for this case since a turbulent model was not used.

$$T = T_l + T_t \quad (15)$$

$$T_l = \mu[\nabla v + \nabla v^T - \frac{2}{3}(\nabla \cdot v)I] \quad (16)$$

The velocity gradient tensor ( $\nabla v_f$ ) is written in terms of the cell velocities in order to evaluate the stress tensor (T). The velocity gradient tensor at the interior face is then written as follows:

$$\nabla v_f = \Delta v \otimes \bar{\alpha} + \overline{\nabla v_f} - (\overline{\nabla v_f} \cdot ds) \otimes \bar{\alpha} \quad (17)$$

$$\Delta v = v_1 - v_0 \quad (18)$$

$$\overline{\nabla v_f} = (\nabla v_0 - \nabla v_1)/2 \quad (19)$$

Where  $\nabla v_0$  and  $\nabla v_1$  are computed (explicitly) velocity gradient tensor in the cells. For the boundary face the no-slip condition is used. An unsteady, implicit, second order solver was used to solve the Navier-Stokes equation with a time-step of 0.005 sec. The following boundary conditions were imposed on the boundaries: inlet unsteady stagnation pressure on the Innominate Artery face and outlet unsteady mass flow rate on the Right Carotid Artery and Right Subclavian Artery. These boundary conditions were calculated using a 1-D lumped parameter model described in the section 3.4 . The *floating* morpher boundary type method was used for the Innominate, Right Carotid, and Right Subclavian faces. This method allows for the boundaries to be only a function of solid domain boundary conditions.

Table 3: Problem size for fluid domain models

Model	Cells
Aorta: 3-layer-composite	27764
Bifurcation: 3-layer composite	91160

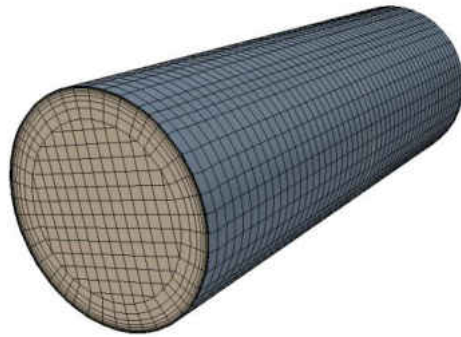


Figure 6: Aorta fluid mesh



Figure 7: Bifurcation fluid mesh

### 3.3 Fluid structure interaction coupling

This FSI contains two domains  $\Omega^S$  and  $\Omega^F$  for the solid and fluid respectively. These two domains do not overlap and are share by a common interface  $\Gamma$ . The information exchanged between these two domains are the pressure  $p$  (traction vector: wall shear stress and static pressure) from the fluid domain and the displacement  $d$  (nodal displacement) from the solid domain for this particular case. The exchanged of these unknowns ( $p$  and  $d$ ) occurs at the shared interface and thus becoming the coupling of the solid and fluid domains (Kuttler & Wall, 2008). Kinematic and dynamic continuity are both fulfilled at all times during the coupling process. In the case of non-slip conditions at the interface  $\Gamma$

$$u_\Gamma = \frac{d}{dt}(\mathbf{d}_\Gamma) \text{ and } \sigma_\Gamma^S \cdot \mathbf{n} = \sigma_\Gamma^F \cdot \mathbf{n} \quad (20)$$

The stresses equal at the deformed interface based on the kinematic continuity where  $\mathbf{n}$  is the time dependent interface normal.  $\mathbf{d}_\Gamma$  represents the interface displacement. The interface displacement changes the interface position as such  $\mathbf{x}_\Gamma = \mathbf{x}_{0,\Gamma} + \mathbf{d}_\Gamma$ . (Kuttler & Wall, 2008).

#### 3.3.1 Co-simulation between ABAQUS and STAR-CCM+

In order to perform the fluid structure interaction (FSI) for this model the commercial software STAR-CCM+ 7.06 CD-adapco and ABAQUS v6.12 SIMULIA were used. STAR-CCM+ was used to solve the fluid domain and ABAQUS the solid domain in this particular FSI model. Each model was first solved individually (no co-simulation) in order to determine if there were any numerical problems. The co-simulation was carried by the SIMULIA Co-simulation engine. The SIMULIA Co-Simulation Engine is responsible for communication between Abaqus and STAR-CCM+. This Engine allows ABAQUS to perform a run-time coupling with a third

party program (CFD) to solve a multiphysics simulation and multidomain coupling and it runs in the background of the simulation (ABAQUS).

STAR-CCM+ uses a mesh motion called *morphing* in order to deform the interface ( $\Gamma$ ) at the fluid domain in accordance to the imported nodal displacements calculated in ABAQUS. The fluid grid deforms accordingly in order to match the solid structure as well as maintaining a reasonable mesh quality. STAR-CCM+ refers this to as a “topologically constant” operation. The mesh motion in STAR-CCM+ uses a multi-quadric morphing model based on radial basis functions. The *morphing* defines the motion of interior vertices, which originates from the motion of the vertices on the structural surface and the fluid transport equations are solved using the space conservation law in order to account for the motion of the mesh (STAR-CCM+).

In order to utilize the SIMULIA Co-Simulation Engine the ABAQUS input file has to be modified with the following script: `*CO-SIMULATION, NAME=<>, PROGRAM=MULTIPHYSICS, CONTROLS=<>`. Under CONTROLS it defines the coupling and rendezvousing schemes that controls the co-simulation. The MULTIPHYSICS program allows exchange data with third-party analysis programs that support the SIMULIA Co-Simulation Engine.

It is important to identify the interface ( $\Gamma$ ) in both the fluid and solid domain. For the solid domain the following script needs to be added:

```
*CO-SIMULATION REGION, TYPE=SURFACE, EXPORT  
  
ASSEMBLY_FSI_INTERFACE, U
```

```
*CO-SIMULATION REGION, TYPE=SURFACE, IMPORT
```

```
ASSEMBLY_FSI_INTERFACE, CF
```

Where the identified interface is called FSI\_INTERFACE and it is exporting U (nodal displacement) and is importing CF (Traction vector: wall shear stress and static pressure) in this particular FSI model.

The next step is to determine the coupling scheme for the exchange of data between ABAQUS and STAR-CCM+. There are currently three choices: JACOBI (explicit parallel coupling), GAUSS-SEIDEL (explicit serial coupling), and ITERATIVE (implicit serial coupling). The script should also be added to the ABAQUS input file as follows: \*CO-SIMULATION CONTROLS, NAME=<>, COUPLING SCHEME=ITERATIVE, SCHEME MODIFIER=LEAD. For this FSI model the ITERATIVE coupling scheme was chosen. The SCHEME MODIFIER is used in the serial coupling and in this case ABAQUS was chosen to lead the co-simulation.

It is also necessary to determine a coupling time step. Thus the next section is added to the \*CO-SIMULATION CONTROLS script: STEP SIZE=IMPORT. There are five choices for the coupling time step: constant, minimum, maximum, import and export. IMPORT was chosen for this particular. This means that ABAQUS can import the suggested coupling time step from STAR-CCM+.

Another parameter that is needed in the SIMULIA Co-Simulation Engine is the controlling of the ABAQUS time incrementation. This parameter is selected as follows: TIME

INCREMENTATION=SUBCYCLE. The SUBCYCLE parameter allows ABAQUS to use its own time incrementation in order to arrive to the target coupling time. This selection is not recommended for implicit coupling since the iterative coupling between the two domains (fluid and solid) will be performed in the last subcycled time step, but it is necessary to use since there is a non-linear deformation in the solid domain. The other option is the LOCKSTEP command which keeps a constant time-step for the solid domain solution. The problem with this choice is that for a non-linear deformation ABAQUS may require smaller time-steps than the prescribed one and thus there is a very high chance that solution will converge.

Another parameter that is added to the co-simulation script is the target time. This parameter is enforced as follows: TIME MARKS=YES. There are two options YES/NO meaning that ABAQUS will exchange data in an exact manner or not (see APPENDIX: DERIVATIONS for final script)

### 3.4 Lumped Parameter Model

An electrical analog was developed, using the Greenfield-Fry's electrical analogy, to simulate pulsatile flow behavior of the human circulatory system. This closed loop circuit was coupled with the fluid structure interaction simulation in order to update the boundary conditions at the inlet and outlets of the fluid domain. This set up allowed for the system (Fluid-solid-lumped parameter model) to behave as complete closed system which closely replicates the behavior of the cardiovascular system (Ceballos, 2011).

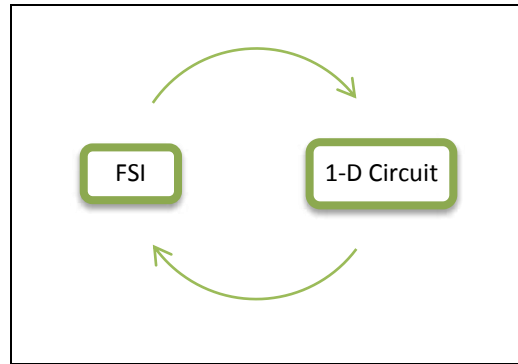


Figure 8: Coupling of FSI and Lump parameter model

This solutions begins from the Navier-Stokes equation using cylindrical coordinates where  $r$  is radial direction variable,  $u$  is the velocity in the x-direction,  $t$  is time,  $\mu$  is the dynamic viscosity,  $P$  is the pressure, and  $\nu$  is the kinematic viscosity.

$$\frac{1}{r} \frac{\partial}{\partial r} \left( r \frac{\partial u}{\partial r} \right) = \frac{1}{\nu} \frac{\partial u}{\partial t} + \frac{1}{\mu} \frac{\partial P}{\partial x} \quad (21)$$



Multiplying and integrating both sides of equation (21) by  $2\pi r dr$  and from zero to  $R$  where  $R$  is the inner radius of the tube respectably leads to equation (22) after some algebraic manipulation.

$$\frac{2}{R} \frac{\partial u}{\partial r} \Big|_R = \frac{1}{\nu \pi R^2} \frac{\partial Q}{\partial t} + \frac{1}{\mu} \frac{\partial P}{\partial x} \quad (22)$$

And for a Newtonian fluid the wall shear stress can be represented as follows:

$$\tau_{wall} = -\mu \frac{\partial u}{\partial r} \Big|_R \quad (23)$$

Taking equations (22) and (23) leads to equation (24) after some manipulation

$$-\frac{\partial P}{\partial x} = \frac{\rho}{\pi R^2} \frac{\partial Q}{\partial t} + \frac{2\tau_{wall}}{R} \quad (24)$$

Equation (24) can be further simplified by assuming a Poiseuille flow which allows the wall shear to be expressed as follows:

$$\tau_{wall} = \frac{8\mu Q}{2\pi R^3} \quad (25)$$

Where  $Q$  is the flow rate and  $R$  the inner radius of the vessel. Equation (24) then becomes

$$-\frac{dP}{dx} = \frac{\rho}{\pi R^2} \frac{\partial Q}{\partial t} + \frac{8\mu Q}{2\pi R^3} \quad (26)$$

Equation (26) can then be expressed as follows

$$-\frac{dP}{dx} = L_u \frac{\partial Q}{\partial t} + R_v Q \quad (27)$$

Where  $L_u$  and  $R_v$  are the vascular inductance and resistance.  $c_u$  and  $c_v$  are constants typically found by experiment. They arise from the assumption that in a Poiseuille flow the wall shear stress is depended on  $Q$  and  $\dot{Q}$

$$L_u = \frac{c_u \rho}{\pi R^2} \quad (28)$$

$$R_v = \frac{c_v 8\mu}{2\pi R^3} \quad (29)$$

In order to express the compliance that occurs on the vessel a capacitor is used as an analogous. Thus the flow rate that passes through the capacitor can be represented as follows.

$$C = \frac{dV/dt}{dP/dt} = \frac{\text{change in volume per change in time}}{\text{change in pressure per change in time}} \quad (30)$$

$$Q = \frac{dV}{dt} = C \frac{dP}{dt} \quad (31)$$

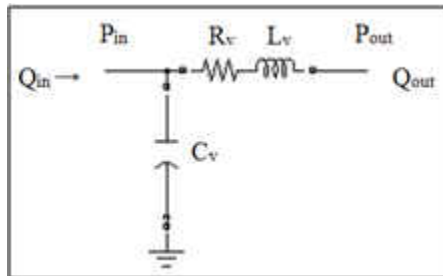


Figure 9: Generic block of vascular bed compartments

For this particular of lump parameter model only the left ventricle of the heart was model. The heart was modeled with a time dependent capacitor which is the driving function of the circuit. The *volume modulus of elasticity* is equal to the reciprocal of the time dependent capacitor which provides the pulsatile flow needed in the circuit.

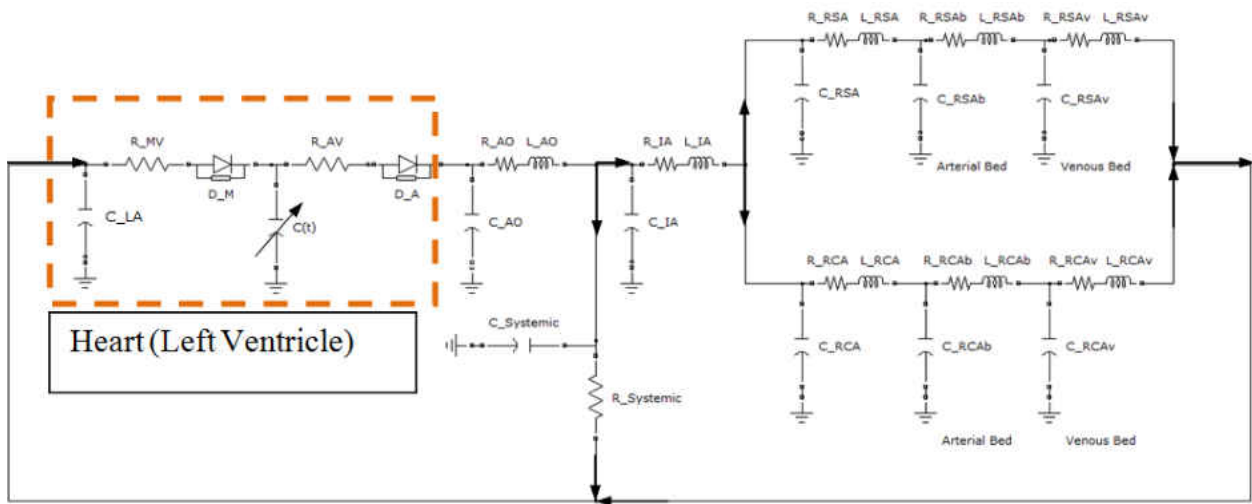


Figure 10: Bifurcation 1-D cardiovascular circuit model

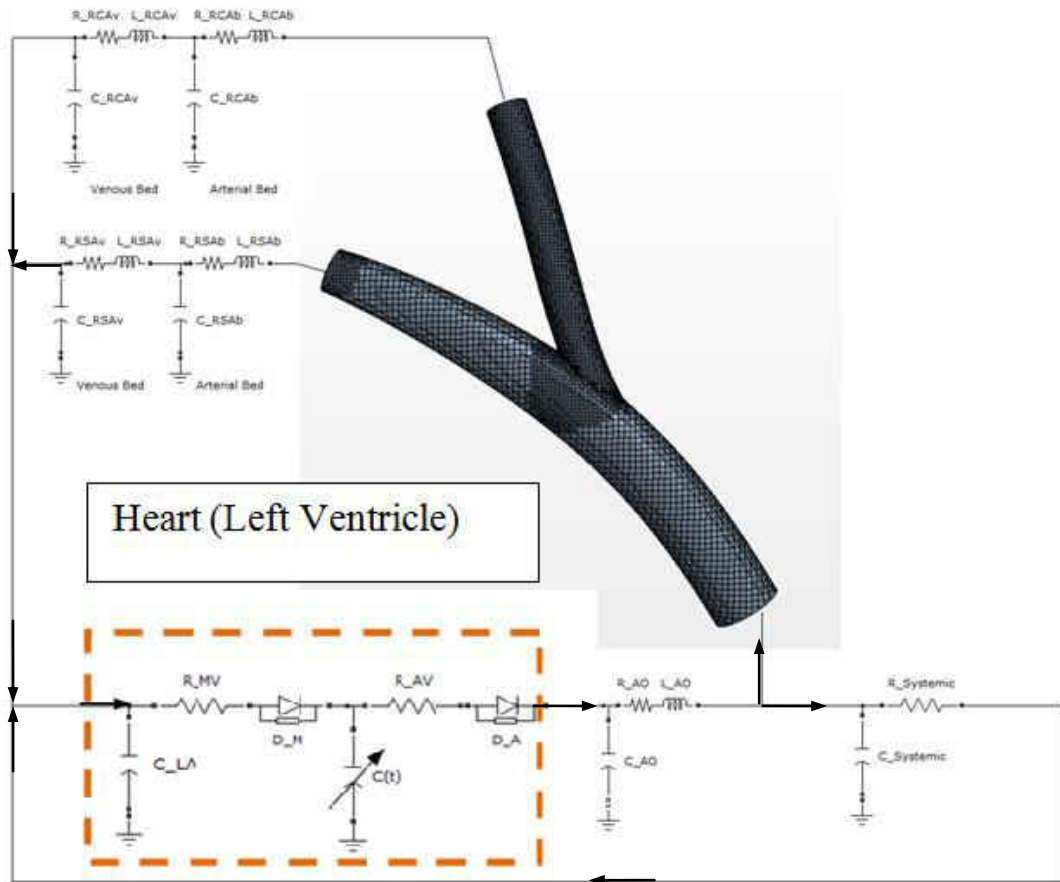


Figure 11: FSI couple with lump parameter model

The time dependant capacitor shown in Figure 10 represents the left ventricle compliance ( $C(t)$ ) which equals the reciprocal of the elastance ( $E(t)$ ). For this research the “double hill” elastance function was used (Simaan, Ferreira, Chen, Antaki, & Galati, 2009).

$$E_n(t_n) = 1.55 * \left[ \frac{\left(\frac{t_n}{0.7}\right)^{1.9}}{1 + \left(\frac{t_n}{0.7}\right)^{1.9}} \right] * \left[ \frac{1}{1 + \left(\frac{t_n}{1.17}\right)^{21.9}} \right] \quad (32)$$

$$t_n = \frac{t}{T_{max}} \text{ and } T_{max} = 0.2 + 0.15 * t_c \quad (33)$$

$$E(t) = (E_{max} - E_{min}) * E_n(t_n) + E_{min} \text{ and } C(t) = 1/E(t) \quad (34)$$

$E_n(t_n)$  represents the normalized elastance as a function of  $t_n$  which is defined in equation (33).  $t_c$  in equation (33) represents the cardiac cycle interval (60/HR and HR is the heart rate). For the values of  $E_{max}$  and  $E_{min}$  2 and 0.06 mmHg/ml were used respectably with a heartbeat of 70 beats per minute. The parameters used to model the left ventricle of the heart are shown in below in Table 4. The  $E(t)$  and  $-\dot{C}(t)/C(t)$  plots in Figure 12 match the plots used in Simaan’s work (Simaan, Ferreira, Chen, Antaki, & Galati, 2009).

For this particular case nineteen first order differential equations were solved using the Runge-Kutta 4<sup>th</sup> order adaptive solver function in MathCAD. The periodic solution was ran for thirteen cycles before it converge The pressure waveform for the ventricular, atrial, and aorta root pressure are shown in Figure 13 as well as the flow rate waveform of the cardiac output. These pressure and flow rate waveform are of similar shape and magnitude as the ones found in Simaan’s study (Simaan, Ferreira, Chen, Antaki, & Galati, 2009).

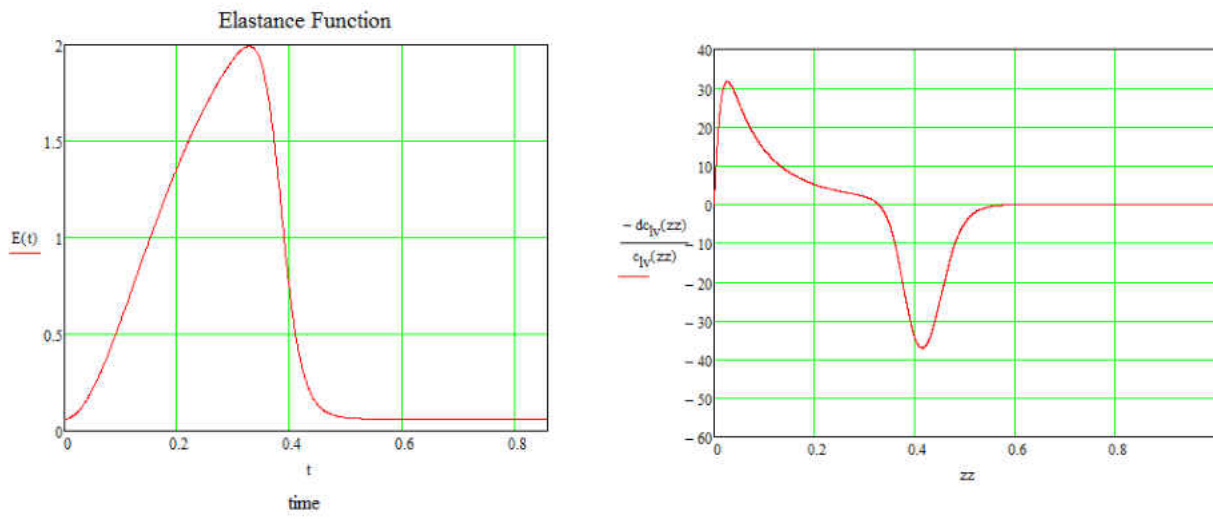


Figure 12: Elastance Function and  $-\dot{C}(t)/C(t)$  over one cardiac cycle

Table 4: Left ventricle heart, aorta, and systemic model parameters

(Simaan, Ferreira, Chen, Antaki, & Galati, 2009) (Ottese, Olufsen, & Larsen, 2004)  
(Lagana, et al., 2005)

Physiological meaning	Value	Units	Parameter
Left Atrial Elastance	0.075	<i>mmHg/ml</i>	C_LA
Mitrial Valve Resistance	0.005	<i>mmHg · s/ml</i>	R_MV
Mitrial Valve			D_M
Left Ventricular Compliance	Time dependant	<i>ml/mmHg</i>	C(t)
Aortic Valve Resistance	0.001	<i>mmHg · s/ml</i>	R_AV
Aortic Valve			D_A
Aorta Capacitance	0.08	<i>ml/mmHg</i>	C_AO
Aorta Resistance	0.0398	<i>mmHg · s/ml</i>	R_AO
Aorta Inductance	0.0005	<i>mmHg · s<sup>2</sup>/ml</i>	L_AO
Systemic resistance	1	<i>mmHg · s/ml</i>	R_systemic
RCA venous bed Inductance	0.001069	<i>mmHg · s<sup>2</sup>/ml</i>	L_RCav
RSA venous bed Inductance	0.001069	<i>mmHg · s<sup>2</sup>/ml</i>	L_RSAv

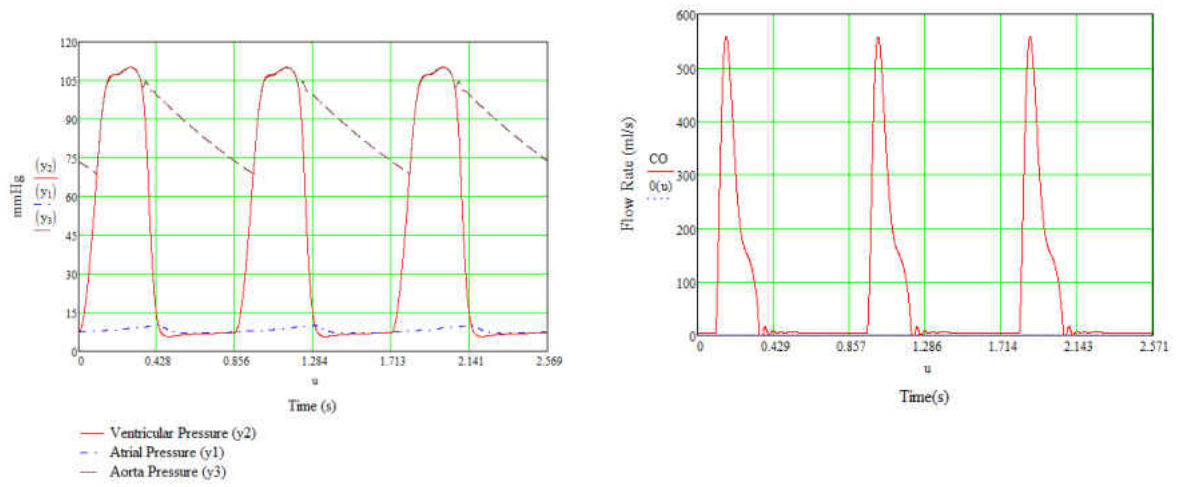


Figure 13: Pressure and Cardiac output

## CHAPTER 4: RESULTS

As mentioned above, the bifurcation compliant model was studied. This model comprises of the brachiocephalic trunk, right carotid and right subclavian arteries. It was then compared to the compliant with Gore-Tex model and the non-compliant model in order to study the changes in the flow field, pressure and wall shear stress. The compliant model ran for twenty FSI-1D circuit iterations before it reached convergence. The final calculated values for the innominate, right carotid and right subclavian arteries are shown in Table 5. Table 6 contains the total flow rate calculated for each of the three models. The arterial and venous beds values are found in Table 7 as well as the systemic resistance and capacitance. The standard deviation and mean of the characteristic impedance of the brachiocephalic trunk, right carotid artery and right subclavian artery were as follows  $0.006$ ,  $0.026$ ,  $0.012$  and  $0.214\text{mmHg} \cdot \text{s/ml}$ ,  $1.134\text{mmHg} \cdot \text{s/ml}$ ,  $0.270\text{mmHg} \cdot \text{s/ml}$  respectively. The percent changed of cardiac output was  $\ll 2\%$ . Figure 14 and Figure 15 show the results of the pressure and flow rate waveforms in the brachiocephalic, right carotid, and right subclavian artery. Figure 16 compares the calculated right carotid artery waveform with a Doppler sample waveform. It can be noticed from Figure 16 the similarities in the calculated waveform and the Doppler sample. The black/white dots represent the peaks and dips of the wave in one cycle. It was also noticed that the total output increased as the models became more rigid. The aorta model was used to test the boundary conditions and material properties applied to the fluid and solid domains. It was also used to validate the FSI simulation. The pressure wave velocity (PWS) in the aorta was calculated for one cycle. It equals  $7.2$  m/s using the parameters given in the methods section which is within range according to Caro (Caro, Pedley, Schroter, & Seed, 2012).



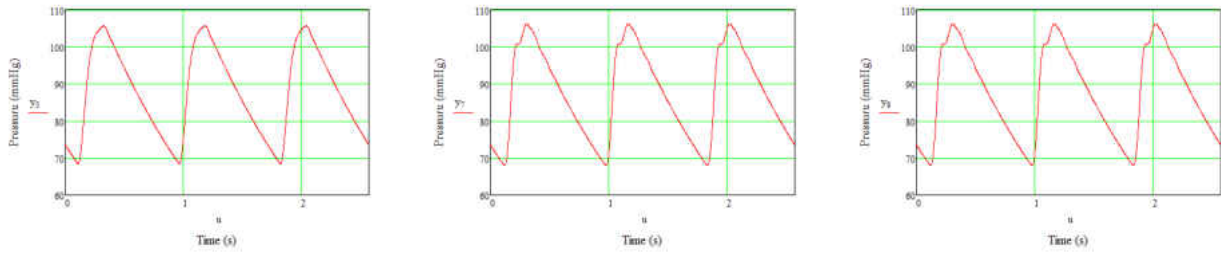


Figure 14: Innominate, Right Carotid, and Right Subclavian Artery Pressure waveform

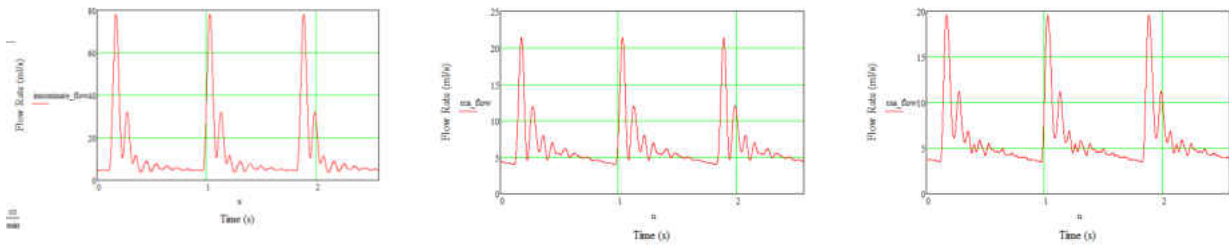
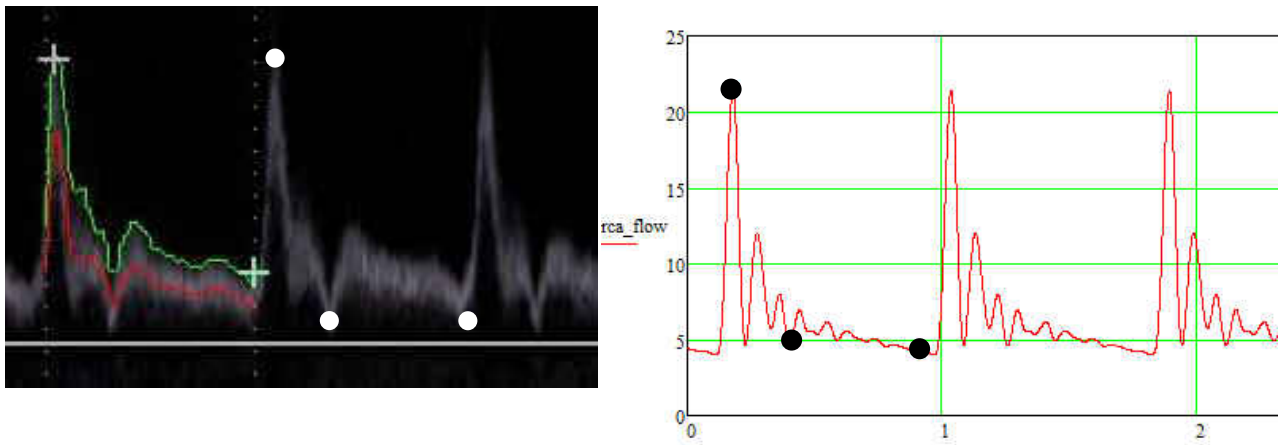


Figure 15: Innominate, Right Carotid, and Right Subclavian Artery Flow rate waveform



(Simens-Healthcare)

Figure 16: Carotid Artery Doppler images and calculated flow rate (ml/s) waveform

Table 5: Calculated resistance, capacitance, and inductance of arteries

Physiological meaning	Value	Units	Parameter
Innominate Artery Resistance	0.015	$mmHg \cdot s/ml$	R_IA
Innominate Artery Capacitance	0.0596	$ml/mmHg$	C_IA
Innominate Artery Inductance	0.002	$mmHg \cdot s^2/ml$	L_IA
Right Carotid Artery Resistance	0.058	$mmHg \cdot s/ml$	R_RCA
Right Carotid Artery Capacitance	0.007	$ml/mmHg$	C_RCA
Right Carotid Artery Inductance	0.006	$mmHg \cdot s^2/ml$	L_RCA
Right Subclavian Resistance	0.018	$ml/mmHg$	R_RSA
Right Subclavian Capacitance	0.059	$mmHg \cdot s/ml$	C_RSA
Right Subclavian Inductance	0.003	$mmHg \cdot s^2/ml$	L_RSA
Aorta Inductance	0.0006	$mmHg \cdot s^2/ml$	L_AO

Table 6: Comparison of total flow rate per cycle between models

		Model		
		Compliant	Compliant with Gore-Tex Patch	Non-Compliant
Output (cc/min)	Right Carotid Artery	457.51	458.23	466.47
	Right Subclavian Artery	417.62	418.27	425.78
	Systemic	4582	4588	4685
	Total	5457.13	5464.5	5577.25

Table 7: Calculated resistance, capacitance, and inductance of arterial and venous beds

Physiological meaning	Value	Units	Parameter
RCA arterial bed Resistance	10.61	$mmHg \cdot s/ml$	R_RCAb
RCA arterial bed Capacitance	0.02	$ml/mmHg$	C_RCAb
RCA arterial bed Inductance	0.02	$mmHg \cdot s^2/ml$	L_RCAb
RSA arterial bed Resistance	11.66	$ml/mmHg$	R_RSAb
RSA arterial bed Capacitance	0.02	$mmHg \cdot s/ml$	C_RSAb
RSA arterial bed Inductance	0.02	$mmHg \cdot s^2/ml$	L_RSAb
Systemic Capacitance	1.05	$ml/mmHg$	C_systemic
Systemic Resistance	1.22	$mmHg \cdot s/ml$	R_systemic
RCA venous bed Resistance	1.51	$mmHg \cdot s/ml$	R_RCAv
RCA venous bed Capacitance	0.007	$ml/mmHg$	C_RCAv
RSA venous bed Resistance	1.66	$ml/mmHg$	R_RSAv
RSA venous bed Capacitance	0.007	$mmHg \cdot s/ml$	C_RSAv

#### 4.1 Comparison between Compliant vs. Compliant with Gore-Tex patch model

The compliant and compliant with Gore-Tex patch models were ran for four cycles (1 cycle = 0.857 secs) each for total time of 3.43 seconds for each simulation. The last iteration of boundary conditions from the 1-D lump parameter was used for these FSI simulations. In order to visualize the difference in the wall shear stress, flow field and pressure gradients four different times were selected within a cycle.

Figure 17 shows the different times selected to represent the comparison between these models.

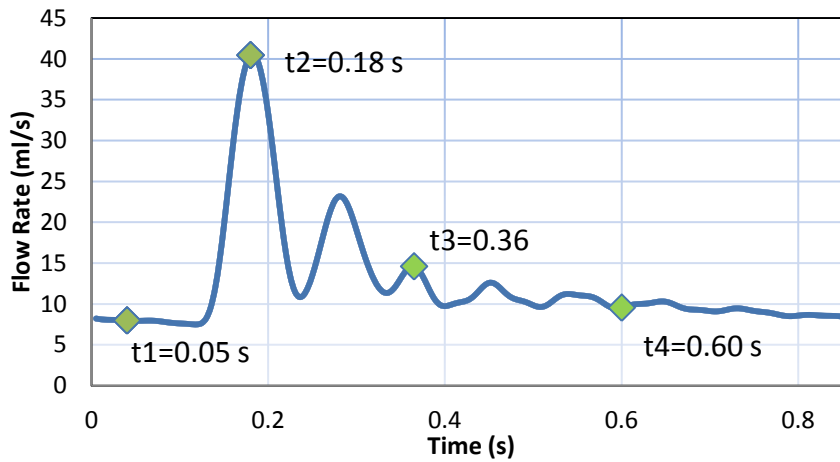


Figure 17: Visualization of flow relative to Innominate artery flow rate

There was an increased in the wall shear stress mainly in the right carotid artery where the patch was placed at  $t=0.18$  sec as it is shown in Figure 18. The max. average wall shear stress value calculated in the Gore-Tex patch area is approx.  $16.5 \text{ dyne/cm}^2$ . It is found in almost the entire right carotid artery. As the flow rate started to decrease at  $t=0.36$  sec a high shear stress

( $\sim 13 \text{ dyne/cm}^2$ ) is noticeable in the transition area between the arterial wall and the patch coming from the bifurcation.

It was noticed that in the cross-section of the right carotid artery in Figure 20 the max. average velocity was  $\sim 42 \text{ cm/s}$  in the patch area compared to  $\sim 30 \text{ cm/s}$  in the compliant model at  $t=0.18 \text{ sec}$ . The flow fields are of similar shape and magnitude for the compliant and compliant with Gore-Tex model in the cross-section view of the right subclavian artery shown in Figure 21. The velocity average calculated at peak time ( $t=0.18 \text{ sec}$ ) shown in Figure 22 was  $\sim 24 \text{ cm/s}$  and  $\sim 32 \text{ cm/s}$  at the innominate root for the compliant Gore-Tex and compliant model respectively. It was also noticed that the velocity increased in the arterial wall-patch transition section. The velocity maintained a maximum value of  $\sim 42 \text{ cm/s}$  throughout the patch section. It then decreased to  $\sim 34 \text{ cm/s}$  after exiting the Gore-Tex patch area. This is shown in Figure 22 at  $t=0.18 \text{ sec}$ . Recirculation was also noticed for both models in Figure 22 at  $t=0.05 \text{ sec}$ . This recirculation was observed at the midsection of the right subclavian artery away from the bifurcation.

The pressure contours in Figure 24 show that there was an increase of pressure at the root of the innominate trunk for the entire cycle in the compliant Gore-Tex model. At  $t=0.05 \text{ sec}$  about half of the innominate trunk was about  $71.13 \text{ mmHg}$  in compliant Gore-Tex model while the compliant model had  $71.1 \text{ mmHg}$ . At  $t=0.18 \text{ sec}$  the pressure in the right carotid artery was approximately  $89.8 \text{ mmHg}$  for most of the artery in patch section. There was a very small pressure gradient variation from the bifurcation to the artery wall-patch transition section. While

the compliant model at  $t=0.18$  sec shows a smoother pressure gradient transition from the bifurcation to the right carotid artery outlet.

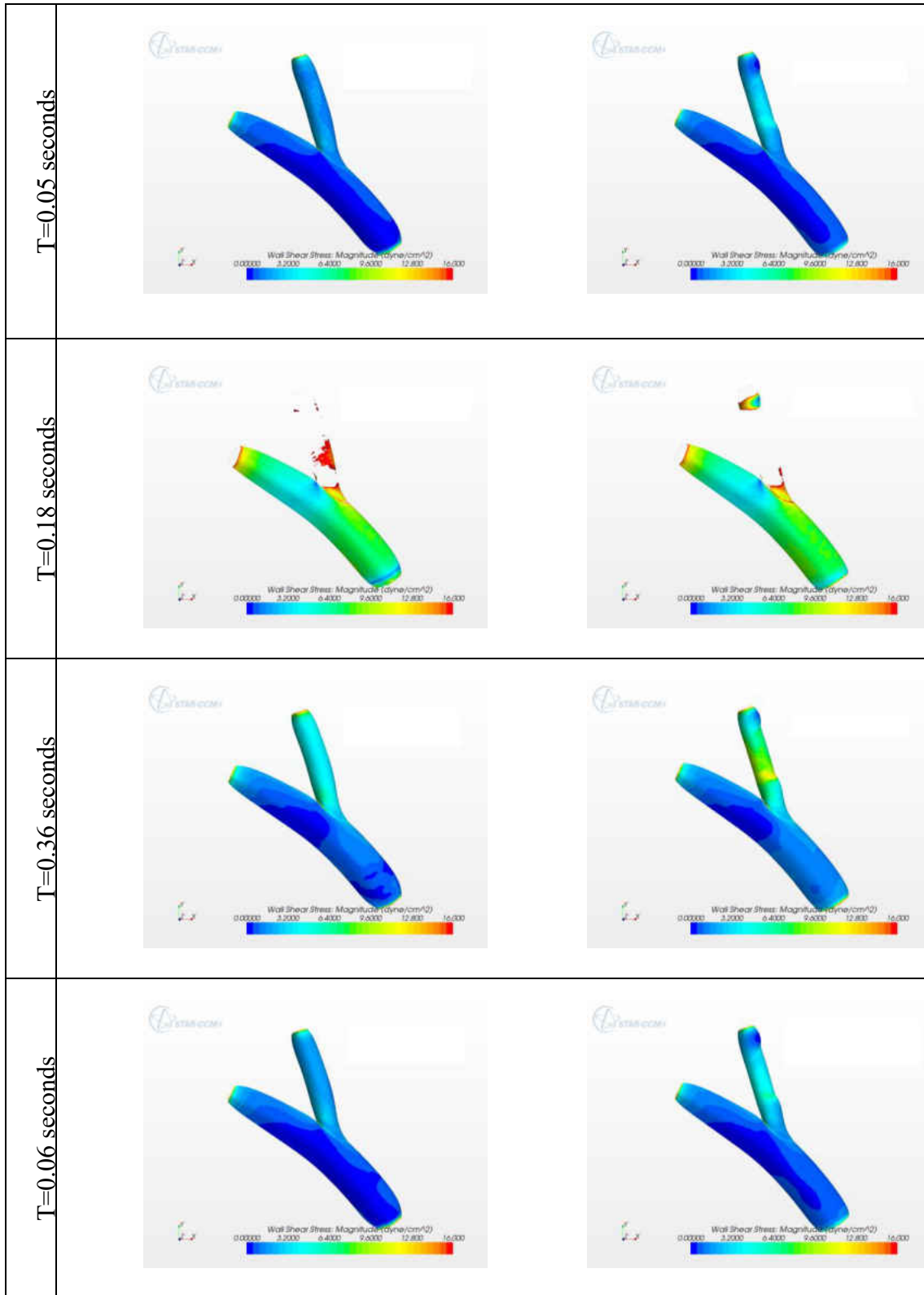


Figure 18: Wall Shear Stress of Compliant and Compliant-Gore-Tex



Figure 19: RSA (right subclavian artery) and RCA (right carotid artery) cross-sections



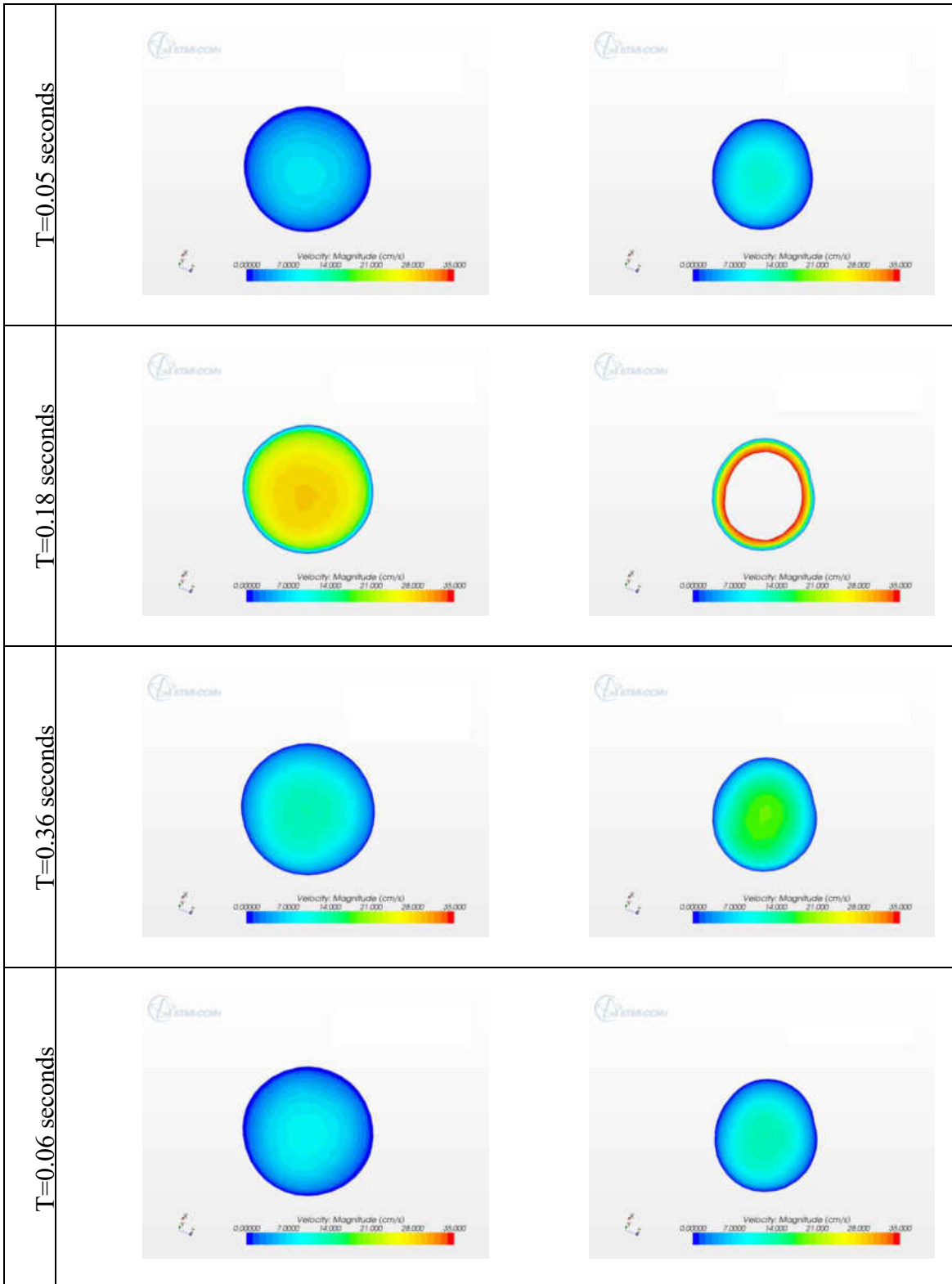


Figure 20: RCA cross-section velocity of Compliant and Compliant-Gore-Tex model

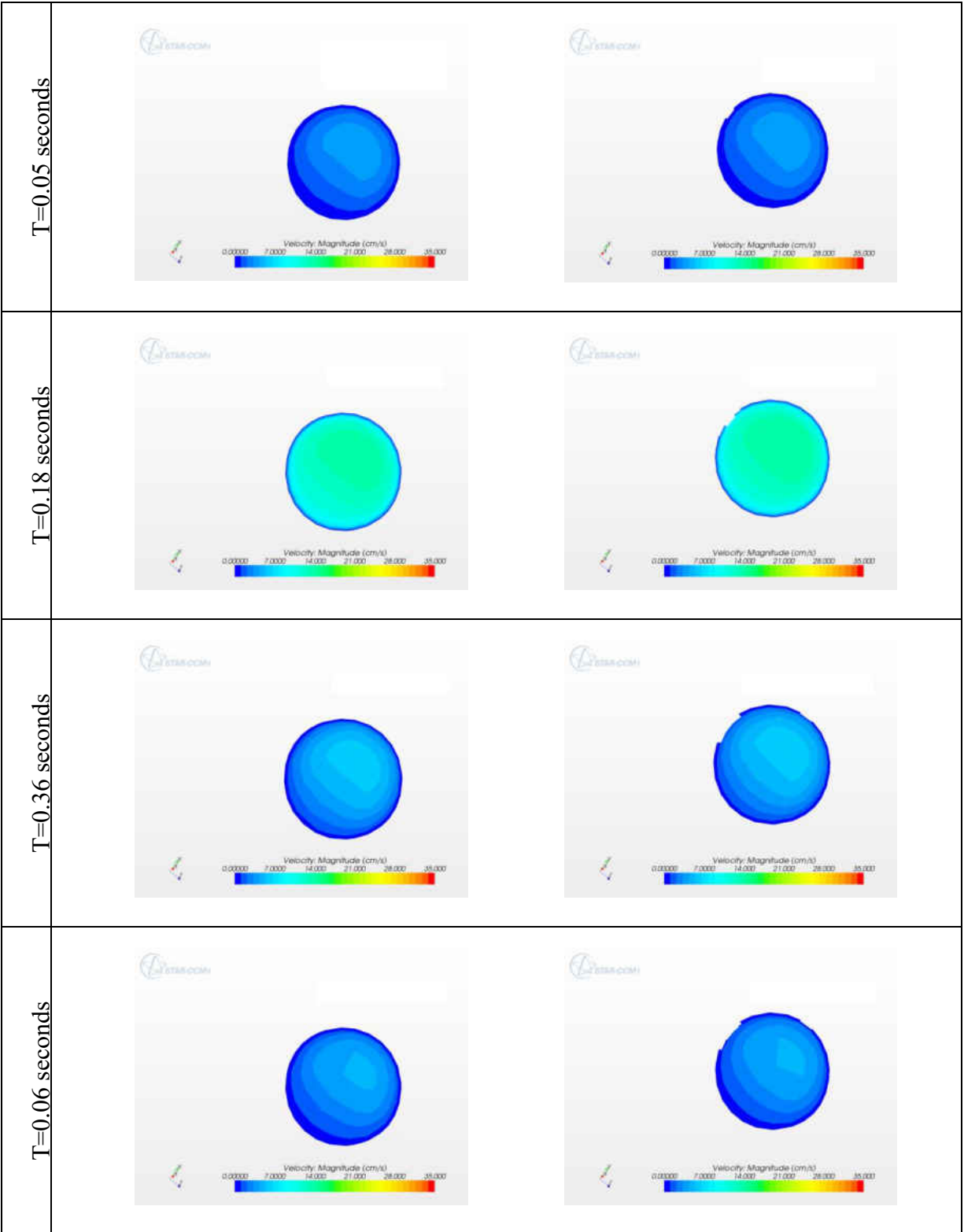


Figure 21: RSA cross-section velocity of Compliant and Compliant-Gore-Tex model

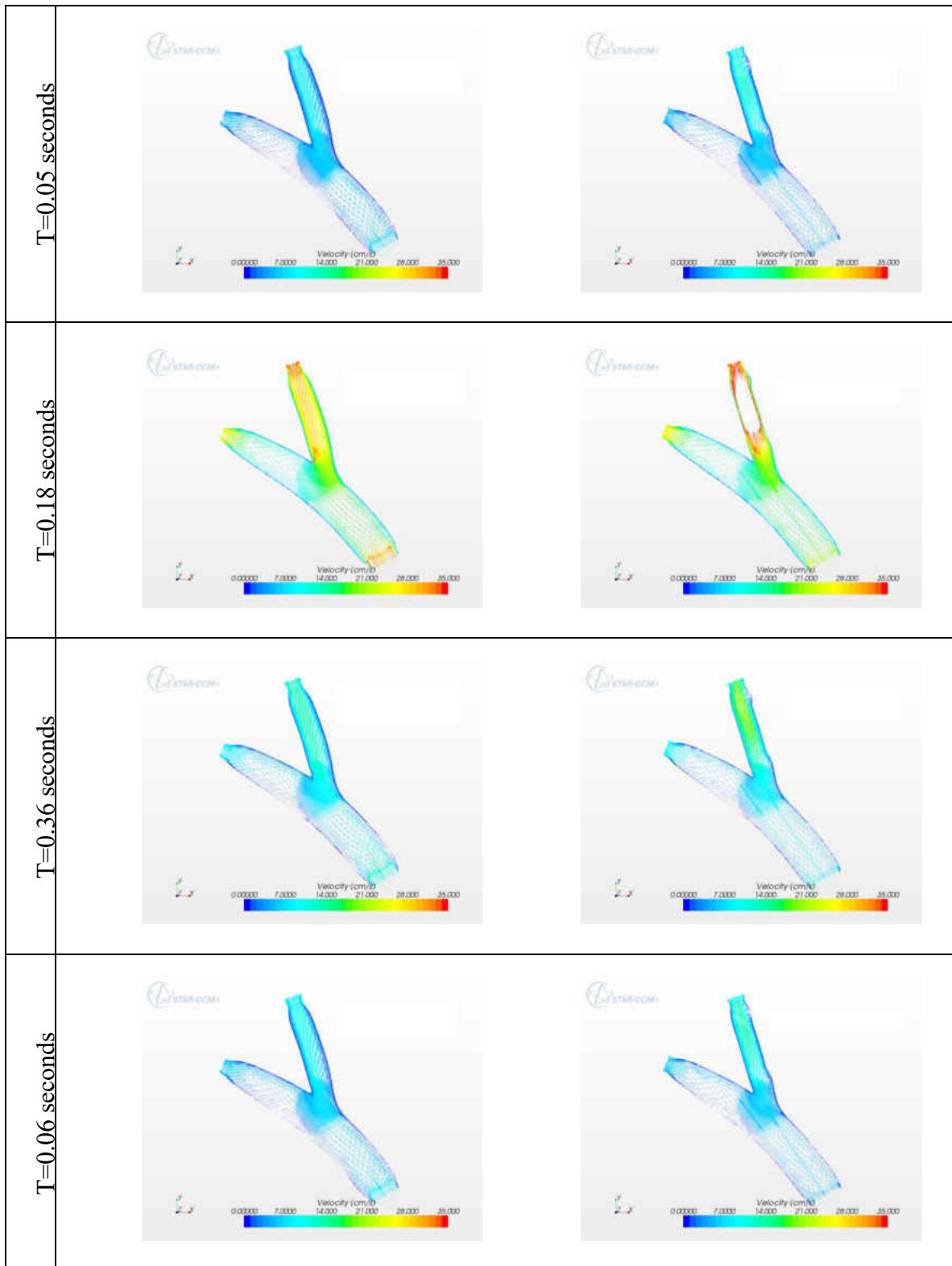


Figure 22: Velocity Field of Compliant and Compliant-Gore-Tex model

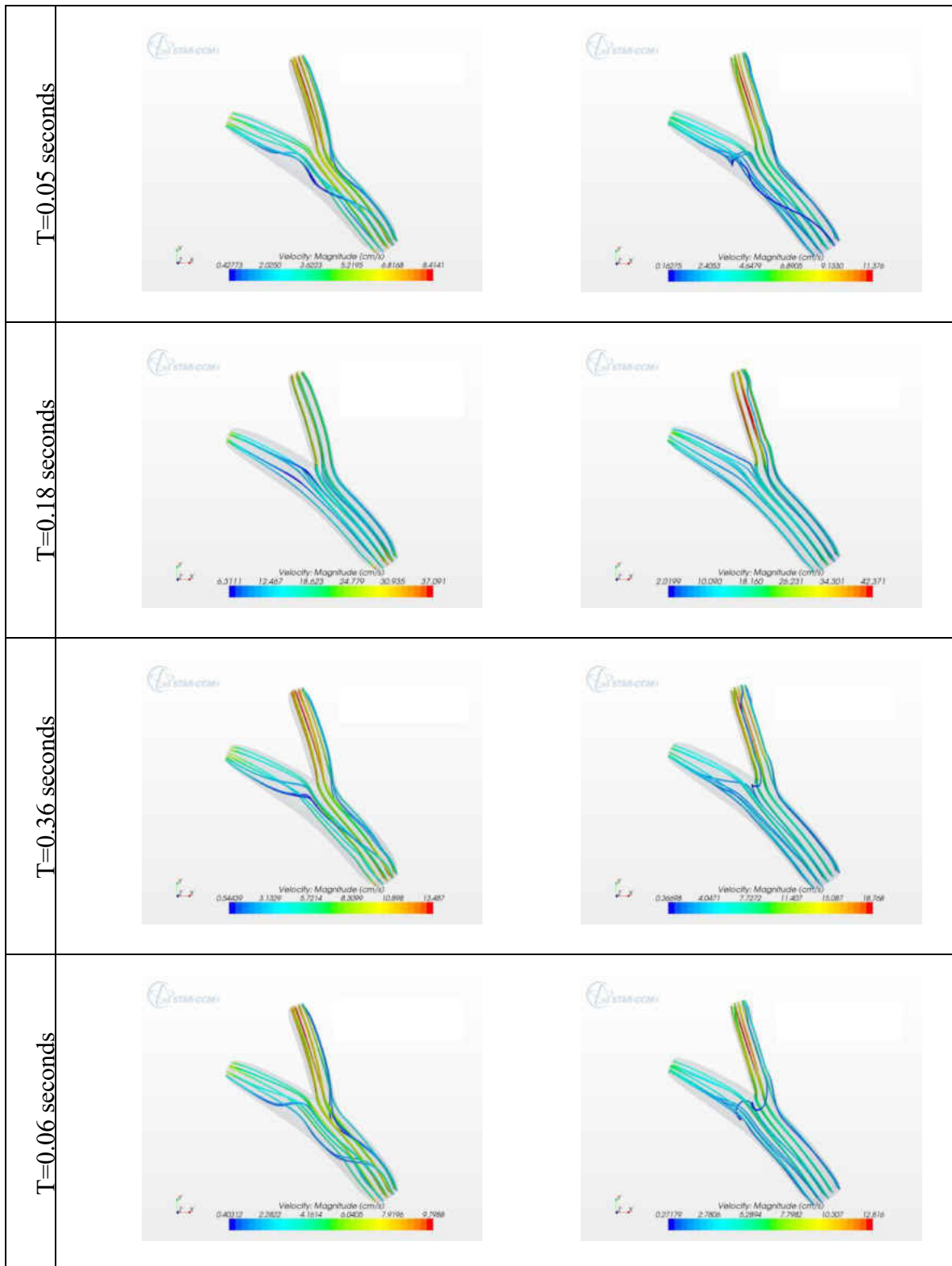


Figure 23: Streamlines velocity magnitude of Compliant and Compliant-Gore-Tex model

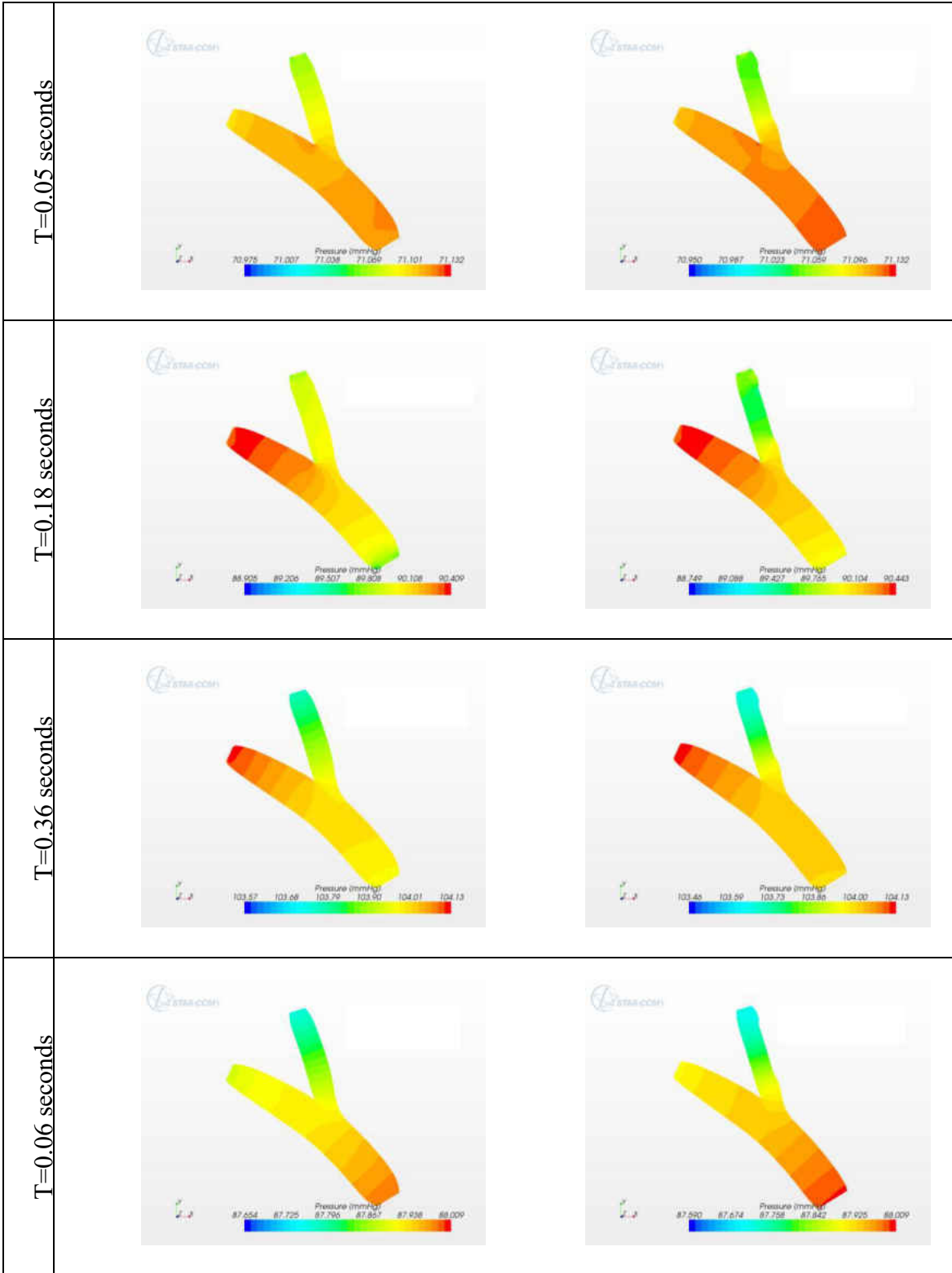


Figure 24: Pressure of Compliant and Compliant-Gore-Tex model

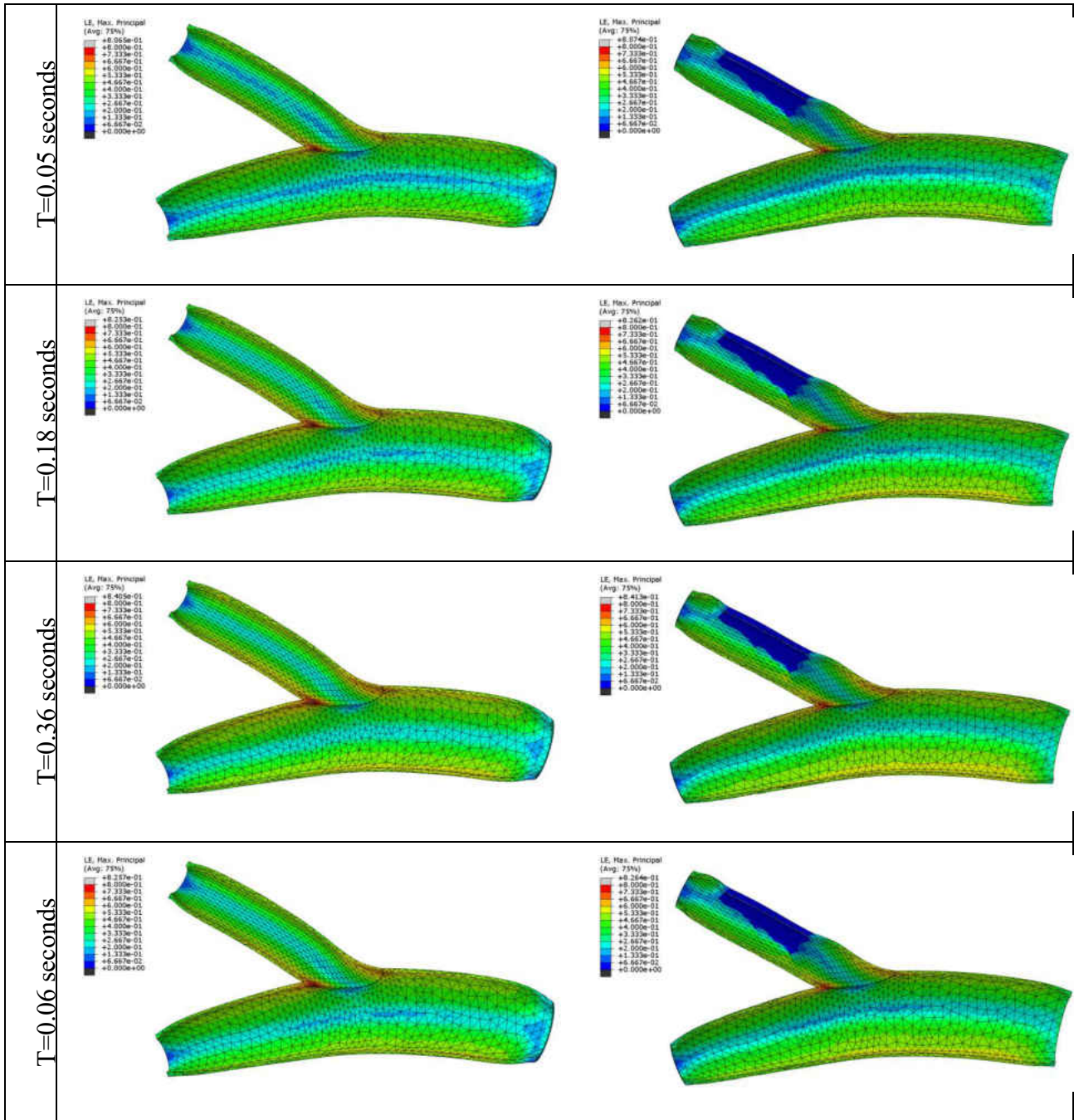


Figure 25: Strain of Compliant and Compliant-Gore-Tex model

Table 8: Von Misses Stress for Compliant model

Von Misses Stress (MPA)			
Time (sec)	IA	RCA	RSA
0.05	0.080	0.042	0.089
0.18	0.100	0.053	0.114
0.36	0.121	0.066	0.140
0.60	0.101	0.054	0.115

Table 9: Von Misses Stress for Compliant with Gore-Tex model

Von Misses Stress (MPA)			
Time (sec)	IA	RCA	RSA
0.05	0.076	0.036	0.090
0.18	0.096	0.048	0.116
0.36	0.116	0.060	0.141
0.60	0.097	0.049	0.116

Table 10: Displacement magnitude for Compliant model

Displacement magnitude (mm)			
Time (sec)	IA	RCA	RSA
0.05	0.034	0.046	0.023
0.18	0.218	0.272	0.150
0.36	0.375	0.515	0.284
0.60	0.234	0.322	0.177

Table 11: Displacement magnitude for Compliant with Gore-Tex model

Displacement magnitude (mm)			
Time (sec)	IA	RCA	RSA
0.05	0.017	0.016	0.010
0.18	0.220	0.070	0.185
0.36	0.402	0.162	0.414
0.60	0.329	0.268	0.440



Table 12: Wall velocity magnitude for Compliant model

Wall velocity magnitude (mm/s)			
Time (sec)	IA	RCA	RSA
0.05	0.727	0.853	0.547
0.18	6.191	9.157	6.378
0.36	1.027	0.683	0.481
0.60	0.943	1.279	0.845

Table 13: Wall velocity magnitude for Compliant with Gore-Tex model

Wall velocity magnitude (mm/s)			
Time (sec)	IA	RCA	RSA
0.05	0.739	0.486	0.467
0.18	4.843	3.862	6.287
0.36	0.899	0.940	0.425
0.60	0.888	0.324	0.591

#### *4.2 Comparison between Compliant vs. non-Compliant model*

The compliant and non-compliant models were ran for four cycles (1 cycle = 0.857 secs) each for total time of 3.43 seconds for each simulation. The last iteration of boundary conditions from the 1-D lump parameter was used for these FSI simulations. In order to visualize the difference in the wall shear stress, flow field and pressure gradients four different times were selected within a cycle.

Figure 17 shows the different times selected to represent the comparison between these models.

There was an increased in the wall shear stress almost throughout the whole bifurcation system at  $t=0.18$  sec as it is shown in Figure 26. The max. average wall shear stress value calculated in the non-compliant model at this time was approx.  $36.5 \text{ dyne/cm}^2$ . As the flow rate started to decrease at  $t=0.36$  sec a high shear stress ( $\sim 16\text{-}13 \text{ dyne/cm}^2$ ) is noticeable throughout the right carotid artery wall.

It was noticed that in the cross-section of the right carotid artery in Figure 27 the max. average velocity was  $\sim 63 \text{ cm/s}$  in the non-compliant model compared to  $\sim 30 \text{ cm/s}$  in the compliant model at  $t=0.18$  sec. The flow fields shown in Figure 28 indicate that there was an increased of velocity in the right subclavian. The non-compliant model shows at  $t=0.18$  sec a maximum velocity of  $\sim 31.5 \text{ cm/s}$  while the compliant model was showing  $\sim 17.5 \text{ cm/s}$  for maximum velocity. The velocity average calculated at peak time ( $t=0.18$  sec) shown in Figure 29 was  $\sim 40 \text{ cm/s}$  and  $\sim 32 \text{ cm/s}$  at the innominate root for the non-compliant and compliant model respectively. It was also noticed that the velocity increased throughout the entire cardiac cycle in

the non-compliant model. A velocity of  $\sim 45$  cm/s was impinging at the bifurcation junction in the non-compliant model compare to  $\sim 20$  cm/s in the compliant model. The velocity maintained a maximum value of  $\sim 40$  cm/s throughout innominate artery and increased as it shifted to the right carotid artery to  $\sim 69$  cm/s. This is shown in Figure 29 at  $t=0.18$ sec. A recirculation was also noticed for both models in Figure 29 at  $t=0.05$ sec. This recirculation was observed at the midsection of the right subclavian artery away from the bifurcation.

The pressure contours in Figure 31: Pressure of Compliant and non-Compliant model at  $t=0.6$  sec are very similar between the compliant and non-compliant model except for the right carotid artery. The non-compliant model showed the pressure to be  $\sim 87.5$  mmHg from the outlet to the midsection of the artery and it gradually increased to 87.7 and 87.8 mmHg as it was approaching to the bifurcation. The pressure contours for the rest of the cycle are different between compliant and non-compliant models. This difference was best shown at  $t=0.18$  sec. The pressure at the root of the innominate it was  $\sim 89.6$  mmHg in the non-compliant model while the compliant model was showing a pressure of  $\sim 90$  mmHg.

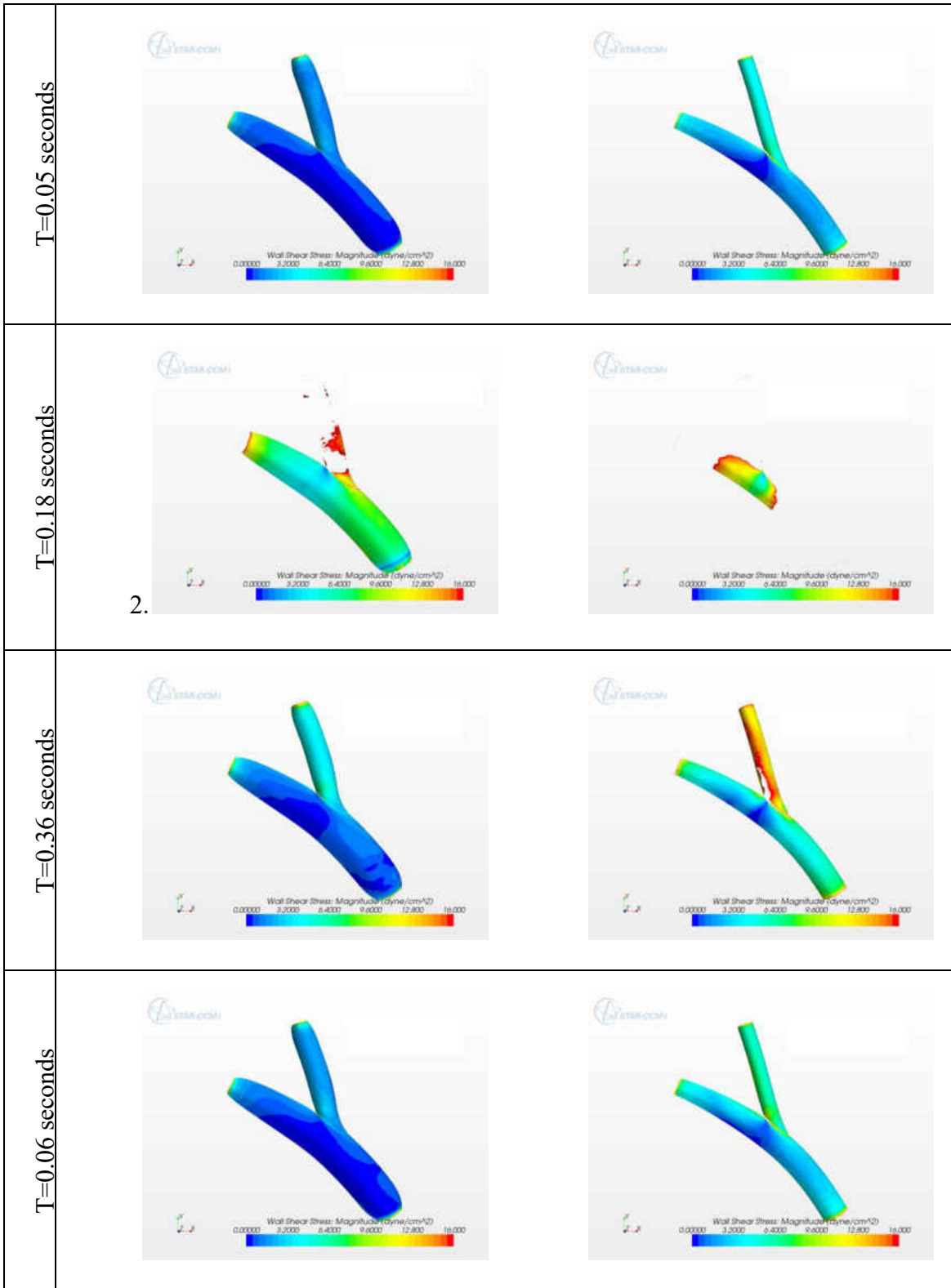


Figure 26: Wall Shear Stress of Compliant and non-Compliant

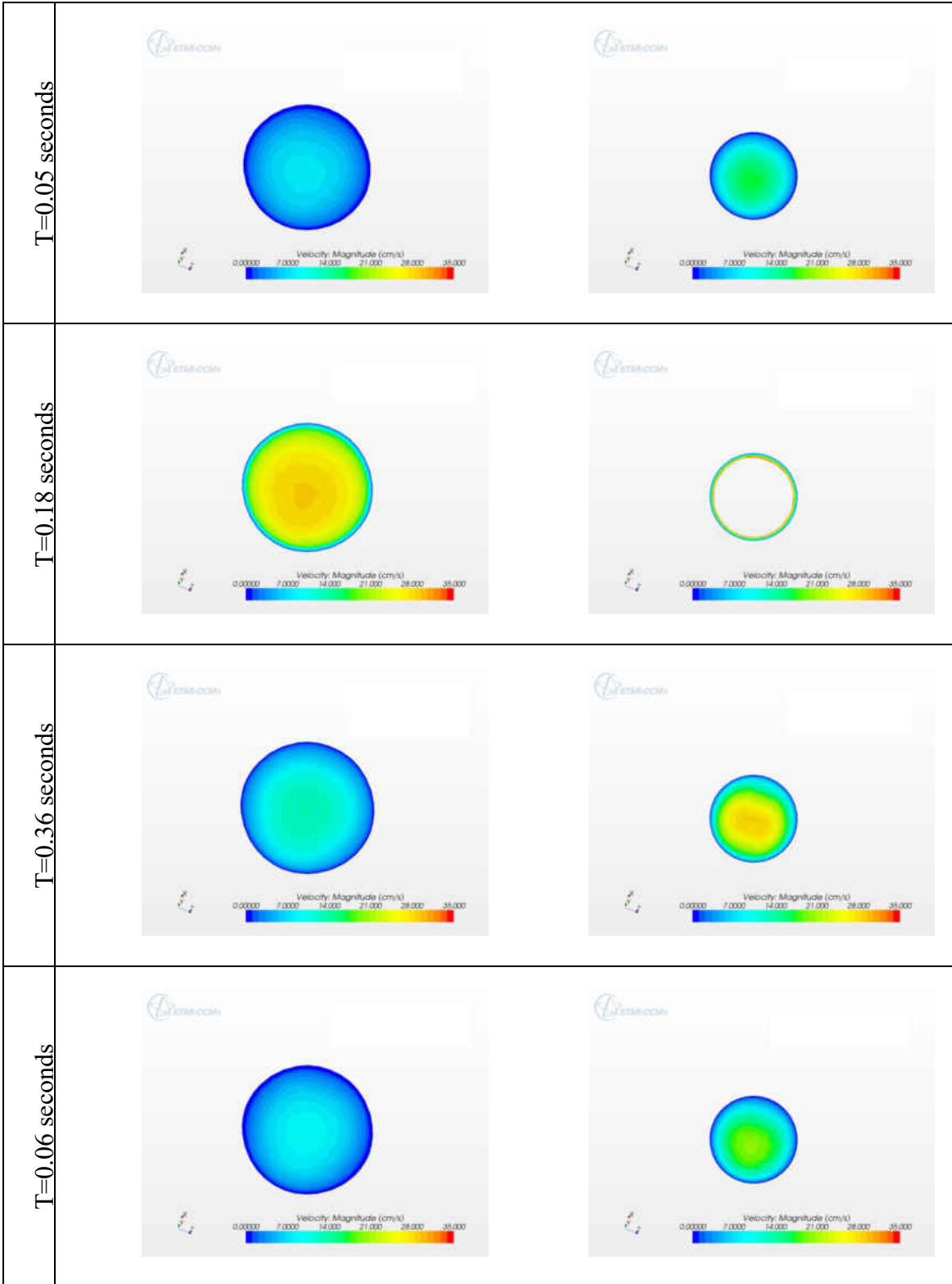


Figure 27: RCA cross section velocity of Compliant and non-Compliant model

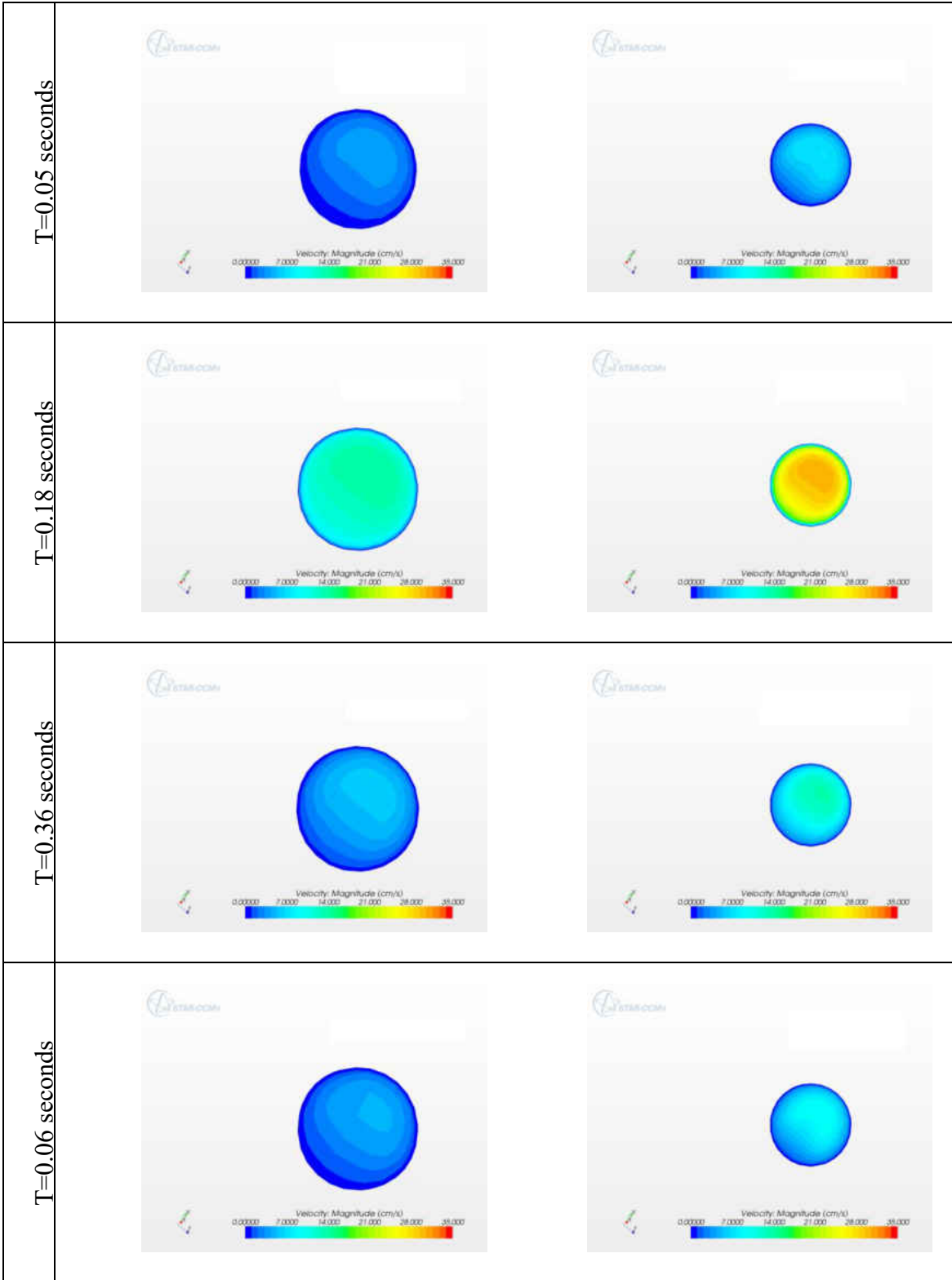


Figure 28: RSA cross section velocity of Compliant and non-Compliant model

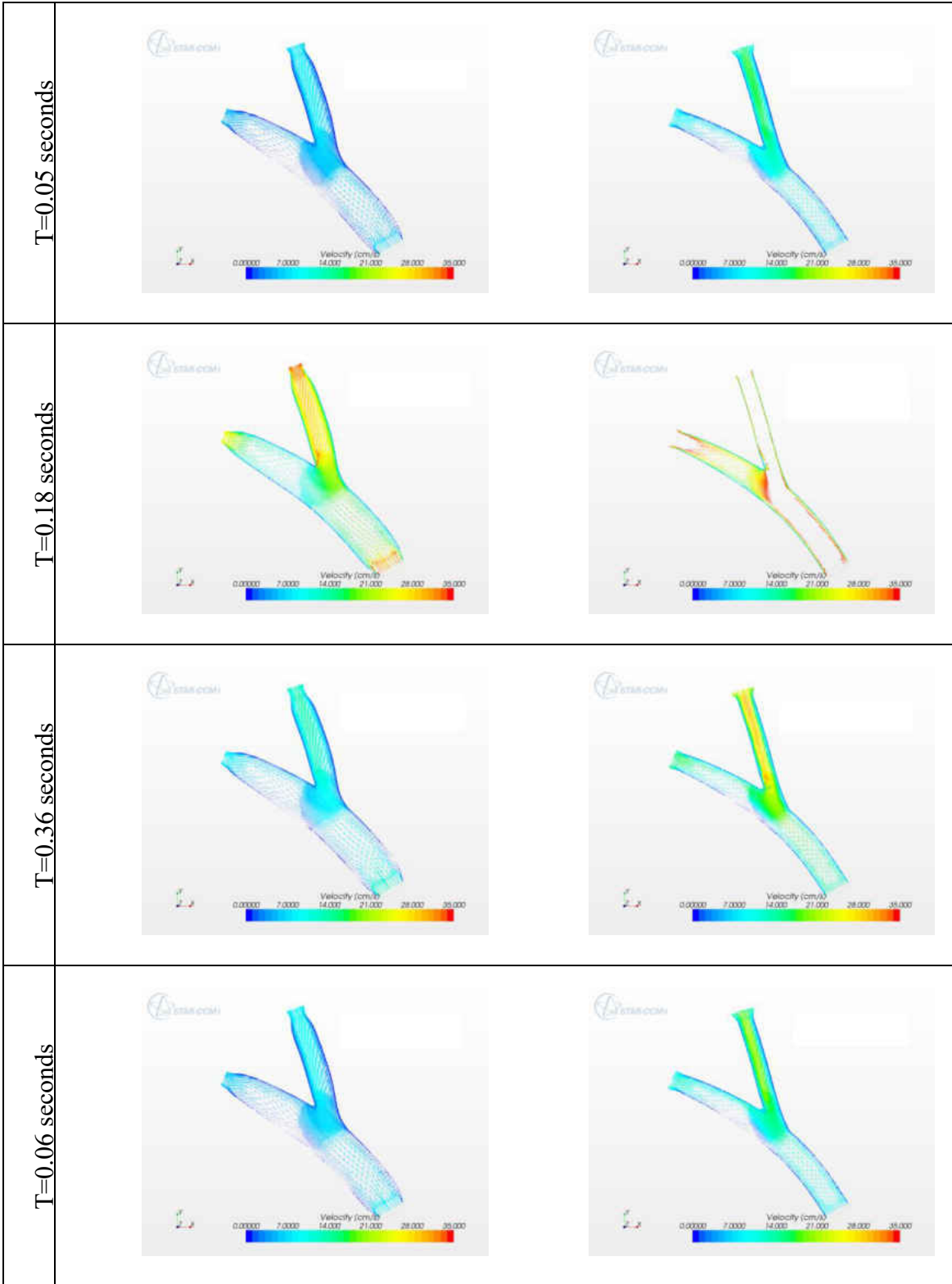


Figure 29: Velocity Field of Compliant and non-Compliant model

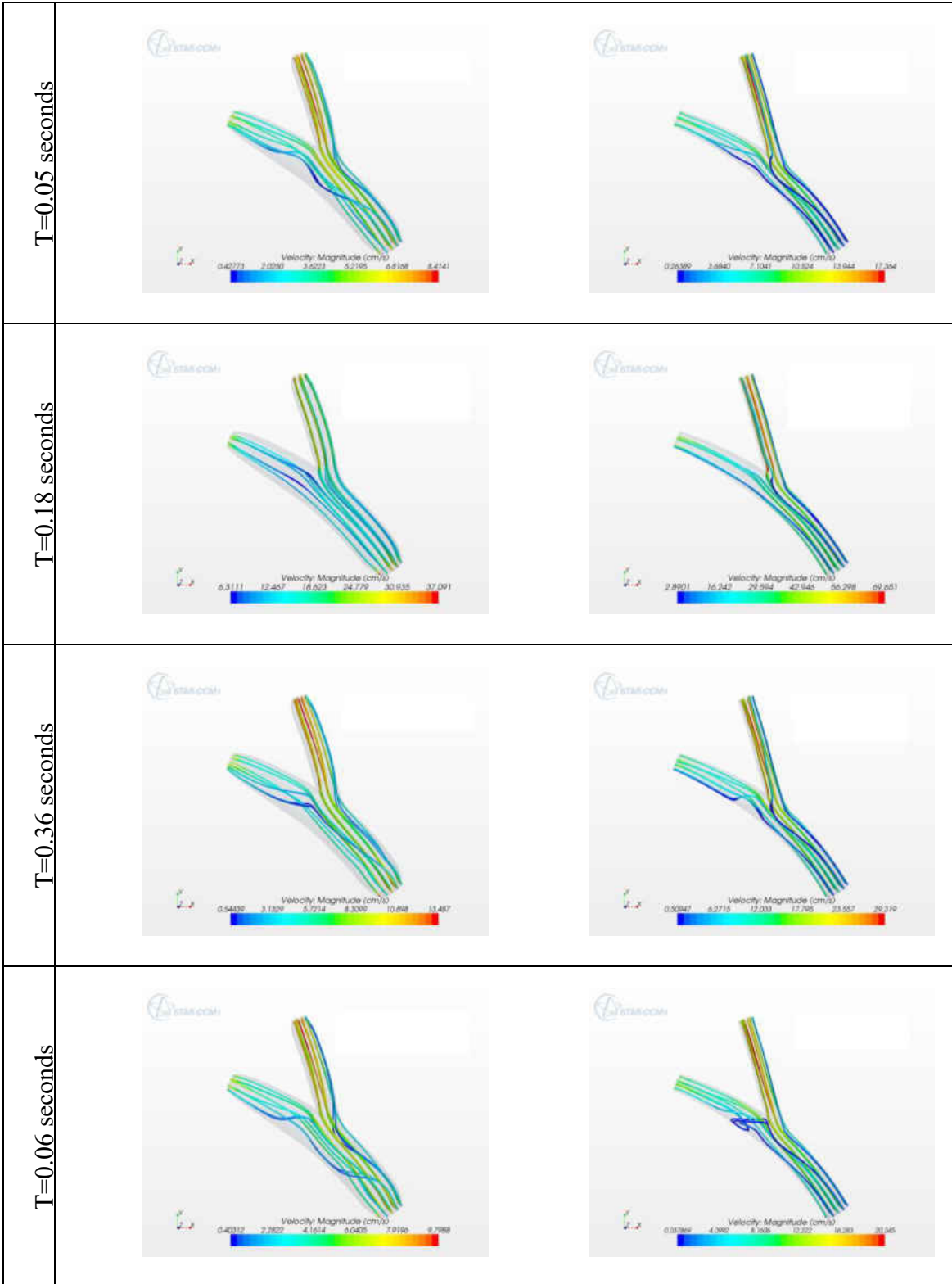


Figure 30: Streamlines velocity magnitude of Compliant and non-Compliant model



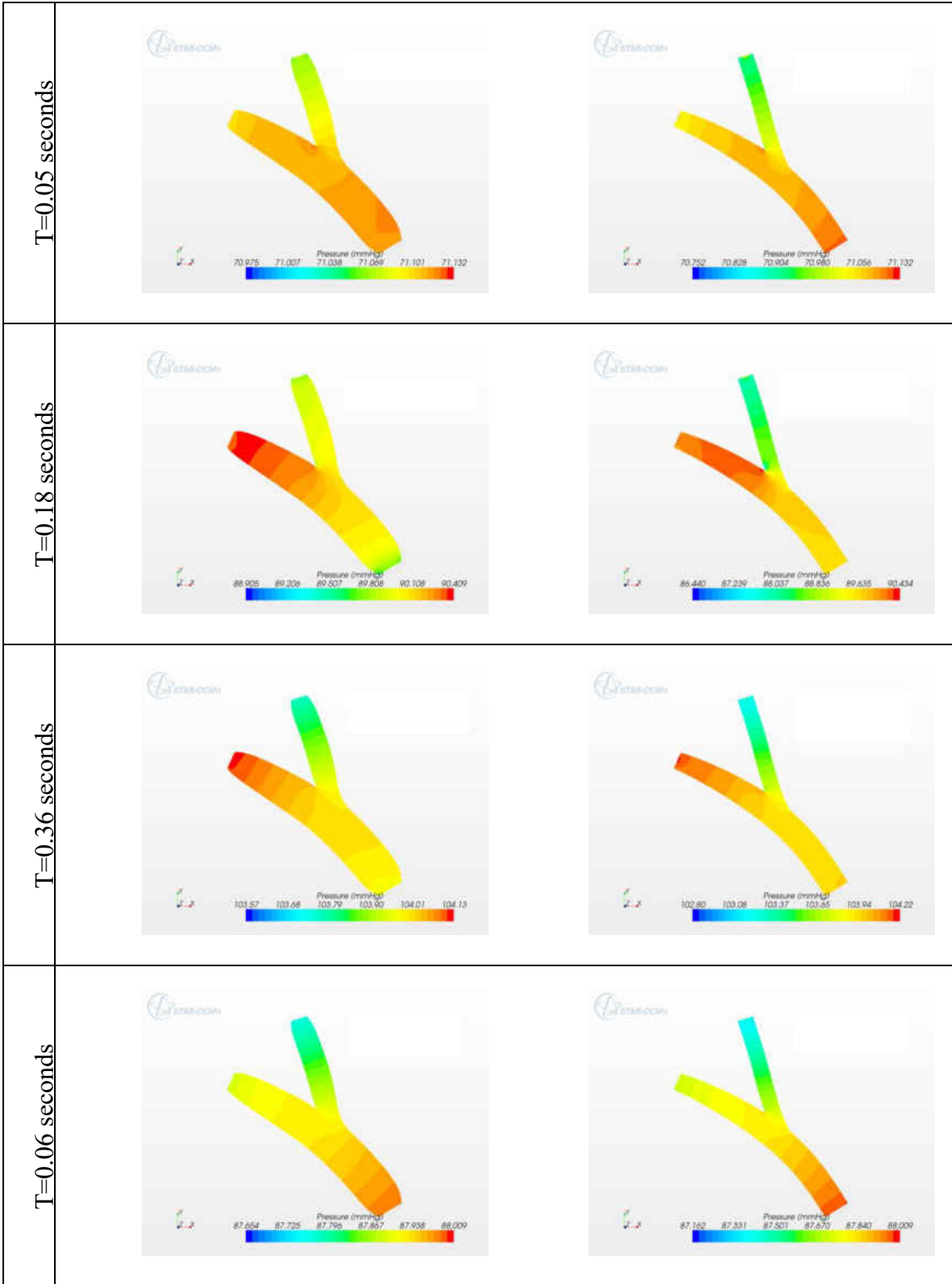


Figure 31: Pressure of Compliant and non-Compliant model

## **CHAPTER 5: CONCLUSION AND FUTURE WORK**

This study shows that multiscale fluid structure interactions with a closed loop lump parameter have an effect on important clinical parameters such as wall shear stress, flow fields and pressures. Furthermore this research shows the behavior of the anisotropic hyperelastic arterial wall has when a material such as Gore-Tex, with much larger elastic properties, is introduced to the solid domain and the impact it has on the flow field. The methodology used in this work brings us a step closer in accurately modeling hemodynamic patterns in large blood vessels when arterial wall motion is taken into consideration. This work will be applied to the computational fluid dynamics modeling of the circulation of congenitally affected cardiovascular systems of neonates, specifically the Norwood and Hybrid Norwood circulation of children affected by the hypoplastic left heart syndrome. Moreover, this study will be used for the optimization of surgical implantation of Left Ventricular Assist Devices (LVAD) cannulae and bypass grafts with the aim to minimize thrombo-embolic events.

Future work should implement a patient specific anatomy instead of a synthetic model in order to provide an investigation to a particular case of study. Also, material properties that can be used to describe an anisotropy hyperelastic model of neonatal blood vessels.

## **APPENDIX: DERIVATIONS**

### *Kinematics*

$F = (J^{1/3} I)\bar{F}$ , where  $F$  is defined into a spherical part  $J^{1/3} I$  and a unimodular part  $\bar{F}$ , and the  $\det \bar{F} = 1$ . Then the Cauchy-Green tensors can be written as:

$$C = F^T F = J^{2/3} \bar{C} \text{ and } \bar{C} = \bar{F}^T \bar{F}$$

$$b = F F^T = J^{2/3} \bar{b} \text{ and } \bar{b} = \bar{F} \bar{F}^T$$

Where  $C$  and  $b$  are the right and left Cauchy-Green tensors, and  $\bar{C}$  and  $\bar{b}$  the modified counterparts (Gasser, Ogden, & Holzapfel, 2006).

### *Bifurcation Boundary Conditions*

```
**
** BOUNDARY CONDITIONS
**
** Name: BC-IA Type: Displacement/Rotation
*Boundary
IA, 1, 1, 2
IA, 2, 2, 2
IA, 3, 3
** Name: BC-RCA Type: Displacement/Rotation
*Boundary
RCA, 1, 1, 1.5
RCA, 2, 2, 1.5
** Name: BC-RSA Type: Displacement/Rotation
*Boundary
RSA, 1, 1, 1.75
RSA, 2, 2, 1.75
```

*Co-simulation final script*

```
*CO-SIMULATION, NAME=AORTA, PROGRAM=MULTIPHYSICS,CONTROLS=Control
*CO-SIMULATION REGION, TYPE=SURFACE, EXPORT
ASSEMBLY_FSI_INTERFACE, U
*CO-SIMULATION REGION, TYPE=SURFACE, IMPORT
ASSEMBLY_FSI_INTERFACE, CF
*CO-SIMULATION CONTROLS, NAME=Control, COUPLING SCHEME=ITERATIVE, SCHEME
MODIFIER=LEAD, STEP SIZE=IMPORT, TIME INCREMENTATION=SUBCYCLE, TIME MARKS=YES
```

## REFERENCES

- ABAQUS, V6.12 .. (n.d.). *Abaqus Analysis User's Manual: 22.5.3 Anisotropic hyperelastic behavior*.
- Brown, A. G., Shi, Y., Marzo, A., Staicu, C., Valverde, I., Beerbaum, P., et al. (2012). Accuracy vs.computationaltime:Translatingaorticsimulationstotheclinic. *Journal of Biomechanics* 45, 516-523.
- Carew, T. E., Vaishnav, R. N., & Patel, D. J. (1968). Compressibility of the Arterial Wall. *Circ Res.* , 23:61-68.
- Caro, C. G., Pedley, T. J., Schroter, R. C., & Seed, W. A. (2012). *The Mechanics of the Circulation*. United Kingdom: Cambridge University Press.
- Ceballos, A. (2011). *A MULTISCALE MODEL OF THE NEONATAL CIRCULATORY SYSTEM FOLLOWING HYBRID NORWOOD PALLIATION*. Orlando: University of Central Florida.
- Gasser, T. C., Ogden, R. W., & Holzapfel, G. A. (2006). Hyperelastic modelling of arterial layers with distributed collagen fibre orientations. *J.R. Soc. Interface* , 3:15-35.
- Holzapfel, G. A., Gasser, T. C., & Ogden, R. W. (2000). A new constitutive framework for arterial wall mechanics and a comparative study of material models. *J. Elasticity* , 61:1-48.
- Kuttler, U., & Wall, W. A. (2008). Fixed-point fluid-structure interaction solver with dynamic relaxation. *Comput Mech* , 43:61-72.
- Lagana, K., Balossino, R., Migliavacca, F., Pennati, G., Bove, E. L., de Leval, M. R., et al. (2005). Multiscale modeling of the cardiovascular system: application to the study of pulmonary and coronary perfusion in the unventricular circulation. *Journal of Biomechanics* 38, 1129-1141.

- Lantz, J., Renner, J., & Karlsson, M. (2011). WALL SHEAR STRESS IN A SUBJECT SPECIFIC HUMAN AORTA — INFLUENCE OF FLUID-STRUCTURE INTERACTION. *International Journal of Applied Mechanics Vol. 3 No. 4* , 759-778.
- Long, C. C., Hsu, M. -C., Bazilevs, Y., Feinstein, J. A., & Marsden, A. L. (2012). Fluid–structure interaction simulations of the Fontan procedure using variable wall properties. *INTERNATIONAL JOURNAL FOR NUMERICAL METHODS IN BIOMEDICAL ENGINEERING*, 28:513-527.
- Nael, K. M., Villablanca, J. P., Pope, W. B., Laub, G. P., & Finn, J. P. (2007). Supraaortic Arteries: Contrast-enhanced MR Angiography at 3.0 T-Highly Accelerated Parallel Acquisition for Improved Spatial Resolution over an Extended Field of View. *Radiology*, 242,600-609.
- Ottese, J. T., Olufsen, M. S., & Larsen, J. K. (2004). *Applied Mathematical Models in Human Physiology*. Philadelphia: Siam.
- Simaan, M. A., Ferreira, A., Chen, S., Antaki, J. F., & Galati, D. G. (2009). A Dynamical State Space Representation and Performance Analysis of a Feedback-Controlled Rotary Left Ventricular Assist Device. *IEEE TRANSACTIONS ON CONTROL SYSTEMS TECHNOLOGY*, Vol. 117, NO.1.
- Siemens-Healthcare*. (n.d.). Retrieved 3 23, 2013, from <http://www.medical.siemens.com>: [http://www.medical.siemens.com/siemens/en\\_US/rg\\_marcom\\_FBAs/images/presskits/ACC\\_2008/USD/X300\\_CCA\\_Doppler.jpg](http://www.medical.siemens.com/siemens/en_US/rg_marcom_FBAs/images/presskits/ACC_2008/USD/X300_CCA_Doppler.jpg)
- STAR-CCM+. (n.d.). STAR-CCM+ User Guide version 7.06.
- Weisbecker, H., Pierce, D. M., & Holzapfel, G. A. (2012). Layer-specific damage experiments and modeling of human thoracic and abdominal aortas with non-atherosclerotic intimal thickening. *Journal of the Mechanical Behavior of Biomedical Materials* , 12:93-106.

Xenow, M., Alemu, Y., Zamfir, D., Einav, S., Ricotta, J. J., Labropoulos, N., et al. (2010). The effect of angulation in abdominal aortic aneurysms: fluid–structure interaction simulations of idealized geometries. *Med Biol Eng Comput.*